

Università degli studi di Milano Bicocca

Dipartimento di Fisica "Giuseppe Occhialini"

Corso di Laurea Triennale in Fisica



# Mapping Dark Matter In Galaxy Clusters Through Kinematic Analysis

Supervisor:

**Dr. Lorenzo Pizzuti**

Candidate:

**Luca Chierichetti**

Student Number:

**846161**

**ACADEMIC YEAR 2024/2025**



*"Remember to look up at the stars and not down at you feet."*  
~ Stephen Hawking

*Un grazie speciale al mio relatore Lorenzo Pizzuti, che mi ha guidato con pazienza, professionalità e grande umanità in questo lavoro e attraverso le meraviglie della cosmologia, rafforzando il mio desiderio di comprendere sempre più a fondo i segreti dell'universo.*



# Abstract

Galaxy clusters are excellent natural laboratories for testing the distribution and physics of dark matter on cosmological scales. In this thesis, a detailed kinematic analyses of the cluster MACS J1206.2–0847 (MACS 1206) is carried out to perform a multi-component reconstruction of the total mass profile. The analysis is based on the high-precision spectroscopic data obtained from the CLASH-VLT collaboration, complemented by the MUSE spectrograph. By means of the MG-MAMPOSST code for kinematic mass determination, the dark matter profile is obtained down to  $\sim 1$  kpc from the center, assuming a generalized Navarro-Frenk-White (gNFW) model. The robustness of the obtained profile has been tested by exploring different parameterizations for the velocity anisotropy, one of the major unknowns in kinematic analyses. We constrained the parameters of the cluster dark matter profile, along with the mass-to-light ratio of the brightest cluster galaxy (BCG) and of the anisotropy profile itself. We found a slope of the dark matter profile  $\gamma = 0.57^{+0.28}_{-0.26}$ , which is slightly smaller than previous determinations in the literature and exhibits a mild ( $\lesssim 2\sigma$ ) tension with the expectation of the standard cold dark matter scenario ( $\gamma = 1$ ). Studies conducted with multi-methodical approaches that combine kinematics and gravitational lensing are necessary to better constrain parameters while significantly improving accuracy. Such analyses are crucial to better understand the nature of dark matter and its role in galaxy clusters.



# Contents

<b>Abstract</b>	<b>i</b>
<b>List of figures</b>	<b>vi</b>
<b>List of tables</b>	<b>vi</b>
<b>1 Introduction to the <math>\Lambda</math>CDM Model</b>	<b>3</b>
1.1 Introduction to cosmology . . . . .	3
1.2 Friedmann equations . . . . .	5
1.3 Perturbations and their evolution . . . . .	8
1.3.1 Linear perturbation . . . . .	8
1.3.2 Relativistic perturbation . . . . .	12
1.3.3 Non linear perturbation . . . . .	14
1.4 Summary of $\Lambda$ CDM model . . . . .	15
<b>2 Dark Matter Properties</b>	<b>19</b>
2.1 Experimental Evidence for the Existence of Dark Matter . . . . .	19
2.1.1 First Evidence by Zwicky . . . . .	19
2.1.2 Rotation Curves . . . . .	20
2.2 Navarro-Frenk-White Dark Matter Density Profile . . . . .	23
2.3 Cusp-core problem . . . . .	27
2.3.1 Baryonic solution . . . . .	27
2.3.2 Cosmological solution . . . . .	28
2.4 Missing satellite problem . . . . .	31
<b>3 Galaxy clusters</b>	<b>33</b>
3.1 Structure of galaxy clusters . . . . .	33
3.1.1 Intra Cluster Medium (ICM) . . . . .	33
3.1.2 Brightest Cluster Galaxy (BCG) . . . . .	35
3.1.3 Galaxies . . . . .	36
3.2 Mass reconstruction . . . . .	37

3.2.1	Mass reconstruction from X-ray observations . . . . .	38
3.2.2	Mass reconstruction with lensing . . . . .	38
3.3	Mass reconstruction with kinematics of member galaxies . . . . .	44
3.3.1	Vlasov equation . . . . .	44
3.3.2	Jeans equation . . . . .	45
3.4	CLASH and the CLASH–VLT program . . . . .	47
3.4.1	MACS 1206 . . . . .	48
<b>4</b>	<b>Analysis with MG-MAMPOSSt code</b>	<b>51</b>
4.1	Kinematic analysis of MACS 1206 . . . . .	54
4.2	Results . . . . .	57
<b>5</b>	<b>Conclusions</b>	<b>63</b>

# List of Figures

1.1	Evolution of universe in different regime	8
1.2	Evolution of cosmic components	9
1.3	CMB image obtained by the Planck satellite	9
1.4	Millenium simulation of cosmic structure	14
1.5	Simulations in different regime	15
1.6	Hubble tension	16
2.1	Rotation curve of a galaxy	21
2.2	CMB power spectrum	22
2.3	Evidence for the universal NFW density profile	24
2.4	Rotation curve of M33	26
2.5	Comparison between NFW and Einasto profiles	26
3.1	Multi-wavelength observations of galaxy cluster Abell 2744	34
3.2	Galaxy distribution	37
3.3	Scheme of gravitational lensing	40
3.4	Weak lensing	42
3.5	Einstein ring around NGC 6505 photographed by Euclid	43
3.6	Galaxy cluster MACS 1206 by HST	49
4.1	Flux diagram MG-MAMPOSSt	52
4.2	Fit for number density density for MACS 1206	53
4.3	Projected space phase for MACS 1206	55
4.4	Marginal distributions of parameters in the BP model with free $r_\beta$	59
4.5	Mass decomposition with BP model and free $r_\beta$	60
4.6	Comparison between anisotropy profile for each anisotropy model and $r_\beta$	61

# List of Tables

3.1	Principal parameters about cluster MACS 1206 . . . . .	49
4.1	Fit for $\beta$ profile . . . . .	54
4.2	Free parameters and relative bounds for MG-MAMPOSST analysis	56
4.3	Results of analyses with MG-MAMPOSST for MACS 1206 . . . . .	57

# Introduction

After the publication of Einstein's theory of General Relativity in 1916 and Hubble's studies in 1929 on the redshift of galaxies, our conception of the universe changed profoundly. These revolutionary theories, supported by extensive experimental evidence, have established the  $\Lambda$ CDM model as the standard framework for modern cosmology. Today, scientists describe the large-scale structure of the universe through three main components: baryonic matter, dark matter, and dark energy. Dark matter appears to hold galaxies together by providing a significant contribution to gravitational forces, while dark energy plays a crucial role in driving the expansion of the universe. Since dark matter makes up approximately 25 % of the universe and dark energy around 70 %, new methods are required to provide an accurate description of the universe and, in particular, of cosmological phenomena.

Our goal is to explore a new approach to infer dark matter properties and, in particular, its distribution in galaxy clusters. To achieve this, we use dynamical observations over a sample of galaxy clusters, along with a specific code: Modify Gravity - Modelling Anisotropy and Mass Profiles of Observed Spherical Systems (also called MG-MAMPOSST) to analyze galaxy clusters and fit the data.

In the first chapter, the standard cosmological model  $\Lambda$ CDM is introduced with fundamental concepts. Following, perturbations and their evolutions in time are described in different regimes. Finally, the observations that confirm the standard cosmological model have been made explicit and the tensions currently present within it.

In the second chapter, principal experimental evidences of the existence of dark matter are described. Subsequently, some popular models for the density profile of dark matter halos are introduced; a specific focus is given to the Navarro-Frenk-White profile and its generalization, which will be used later on to infer the inner slope of the dark matter distribution in clusters. Thereafter, the most important problems of the cosmological standard model are examined, giving us the possibility to understand more about the different types of dark matter such as warm dark matter, self-interacting dark matter, and baryonic solutions able to provide more information through the interaction with dark matter.

In the third chapter, the internal structure of galaxy clusters is examined by describing their main components: brightest cluster galaxy, intra cluster medium and galaxies. The main methods for determining the mass of a galaxy cluster and the density distribution of dark and baryonic matter have been described; in particular, the determination through X-rays, through gravitational lensing and kinematics. For the purposes of studying the mass profile, the Vlasov and Jeans equations were introduced; together with the latter, the concepts related to numerical density, velocity dispersion and velocity anisotropy were treated. Finally, the CLASH and CLASH-VLT projects are briefly described, in particular the most important information about the MACS 1206 cluster (subject to analysis in the next chapter).

In the fourth chapter, the data collected by the CLASH-VLT project through the MG-MAMPOSSt code are finally analyzed, first providing an explanation on the functioning of the program itself and, subsequently, carrying out the analysis of the kinematics of the MACS 1206 cluster through the aforementioned code. The parameter values determined by the code and the plots are then reported, providing a comparison with the results previously found in the articles dealing with the same galactic cluster.

In the fifth and final chapter, the conclusions about the results found in the previous chapter are therefore presented.

# Chapter 1

## Introduction to the $\Lambda$ CDM Model

In this chapter we are going to introduce the basics for describing and understanding the standard cosmological model. The fundamental components of the universe according to the  $\Lambda$ CDM model and the equations underlying it will be introduced, like Friedmann equations (ref. [32]). Linear and non-linear perturbations in the cosmological standard model are also described and, finally, we will briefly discuss the need to study dark matter in more depth to resolve those tensions still present within the standard cosmological model.

### 1.1 Introduction to cosmology

The  $\Lambda$ CDM model is a well-established framework that describes the universe in cosmological terms. This model accurately explains several observations at different scales, such as Cosmic Microwave Background (CMB hereafter) (ref. [1], [76]) and the large-scale structure of the universe. In cosmology, we assume the following principles:

1. *Copernican Principle*

There is no privileged system from which to observe the universe.

2. *Cosmological Principle*

The universe can be considered isotropic and homogeneous.

One of the most important solutions of the Einstein field equation is the Friedmann-Lemaître-Robertson-Walker equations (FLRW equations) that give us a metric that we can use to describe the geometry of the universe; this metric can be expressed in spherical coordinates as follows:

$$ds^2 = -c^2 dt^2 + a(t)^2 \left[ \frac{dr^2}{1 - kr^2} + r^2 d\theta^2 + r^2 \sin^2 \theta d\varphi^2 \right], \quad (1.1)$$

which can be rewritten using the solid angle  $d\Omega$  as

$$ds^2 = -c^2 dt^2 + a(t)^2 \left[ \frac{dr^2}{1 - kr^2} + r^2 d\Omega^2 \right]. \quad (1.2)$$

Here,  $t$  is the cosmological time measured by an observer at rest in the comoving system,  $(r, \theta, \varphi)$  are comoving coordinates that do not change with time, and  $a(t)$  is the scale factor that determines the expansion of the universe (which by convention is between 0 and 1). According to equation (1.2), the geometry of the universe is determined by the parameter  $k$ , which can take three possible values:  $-1$ ,  $0$ , or  $+1$ . In other words, two objects do not change their coordinates over time, but space-time itself expands between them.

We can write Hubble's law

$$v = H(t)D, \quad (1.3)$$

where  $H(t)$  is the Hubble parameter, measured with the following equation

$$H(t) = \frac{\dot{a}}{a}. \quad (1.4)$$

It's also common and useful to indicate the Hubble parameter at the present time with  $H_0$  with a value constrained by CMB observations to  $H_0 = (67.66 \pm 0.42) \text{ km s}^{-1} \text{ Mpc}^{-1}$  (ref. [1]).

This Hubble parameter helps us to obtain an estimate of the age of the universe, thanks to the following simple formula

$$t_0 = \frac{1}{H_0} \simeq 14 \text{ Gyr}, \quad (1.5)$$

also known as "Hubble time". This is a very good value, close to the data estimating the age of the universe at 13.8 Gyr.

Now, if we consider a space-time point with coordinates  $(r, \theta, \varphi) = (0, 0, 0)$ , which corresponds to our position, and a second space-time point at  $(r, \theta, \varphi) = (r_\star, 0, 0)$ , we can calculate the distance between them as follows:

$$l = \int_0^{r_\star} dl. \quad (1.6)$$

Using the FLRW metric, we obtain

$$l = \int_0^{r_\star} dl = a(t) \int_0^{r_\star} \frac{dr}{\sqrt{1 - kr^2}} = a(t) \int_0^{r_\star} dr = a(t)r_\star, \quad (1.7)$$

now, differentiating both sides with respect to time, we get

$$\frac{dl}{dt} = \dot{l} = \dot{a} \int_0^{r_\star} \frac{dr}{\sqrt{1 - kr^2}} = \dot{a} \frac{l}{a}, \quad (1.8)$$

where for  $k = 0$  (ref. [17]), the equation simplifies to

$$\dot{l} = \frac{\dot{a}}{a}l \implies v = H(t)D. \quad (1.9)$$

In an expanding Universe, light emitted by distant sources undergoes a phenomenon known as redshift. This effect is conceptually similar to the Doppler effect experienced by sound waves, where the frequency changes due to the relative motion between the source and the observer. However, in the cosmological context, redshift is primarily caused by the expansion of spacetime itself, as described by the scale factor  $a(t)$  in the metric.

Let us consider a light ray emitted at time  $t_e$  by a distant source with wavelength  $\lambda_e$ , and received at a later time  $t_o$  by an observer, who measures a wavelength  $\lambda_o$ . Due to the expansion of the universe during the light's travel, the observed wavelength  $\lambda_o$  will be stretched compared to the emitted one. This leads to the definition of the redshift  $z$  as:

$$1 + z = \frac{\lambda_o}{\lambda_e} = \frac{a(t_o)}{a(t_e)}, \quad (1.10)$$

where  $a(t_e)$  and  $a(t_o)$  are the values of the scale factor at the time of emission and observation, respectively. Thus, the redshift provides a direct measure of how much the Universe has expanded during the propagation of the light.

## 1.2 Friedmann equations

In general relativity, the relation between the space-time and matter/energy is given by Einstein's field equation

$$R_{\mu\nu} - \frac{1}{2}g_{\mu\nu}R + g_{\mu\nu}\Lambda = \frac{8\pi G}{c^4}T_{\mu\nu}, \quad (1.11)$$

where  $R_{\mu\nu}$  is the Ricci tensor,  $g_{\mu\nu}$  is the metric tensor and  $T_{\mu\nu}$  is the stress-energy-momentum tensor. The energy can be described as a perfect fluid characterized by an energy-momentum tensor

$$T_{\mu\nu} = pg_{\mu\nu} + c^2\left(\frac{p}{c^2} + \rho\right)u_\mu u_\nu, \quad (1.12)$$

where  $p$  is the pressure,  $\rho$  is the density of the fluid and  $u^\mu$  is the 4-velocity of the fluid.

To obtain a first approximation, we can simplify the problem and assume that all of the components of the universe are decoupled and they evolve independently.

The conservation equation is given by the application of the covariant derivative with the FLRW metric  $\nabla_\mu T^{\mu\nu} = 0$  with  $\nabla_\mu$  covariant derivative. The result is:

$$\dot{\rho} + 3\frac{\dot{a}}{a}\left(\rho + \frac{p}{c^2}\right) = 0, \quad (1.13)$$

if we assume  $p = \rho w$  with  $w$  a constant equation of state. Substituting in (1.13) and integrating it is possible to find  $\rho(a)$

$$\rho(a) \propto a^{-3(1+w)}, \quad (1.14)$$

so the three scenarios are the following:

- Radiation:  $w = \frac{1}{3}$
- Matter:  $w = 0$
- Cosmological constant ( $\Lambda$ ):  $w = -1$

From the FLRW metric and General Relativity, we derive two fundamental equations, known as the Friedmann equations (ref. [32]):

$$\begin{cases} \left(\frac{\dot{a}}{a}\right)^2 = \frac{8\pi G}{3}\rho - \frac{kc^2}{a^2} + \frac{\Lambda c^2}{3}, \\ \frac{\ddot{a}}{a} = -\frac{4\pi G}{3c^2}(\rho c^2 + 3p) + \frac{\Lambda c^2}{3}. \end{cases} \quad (1.15)$$

These equations determine the evolution of the scale factor as a function of radiation and matter content in the universe. The density is the sum of radiation density, matter density (baryonic and dark matter) and the last term is the dark energy. In (1.15)  $\dot{a}$  represents the time derivative of  $a$ , while  $\rho$  accounts for both matter and radiation density, and  $p$  is the pressure. This set of equations describe the evolution of the universe in terms of the scale factor  $a(t)$  and the parameter  $k$ . It is also very important to note the negative sign in the second equation, as this is the reason why the velocity of expansion can rapidly slow down in a universe without dark matter. Another crucial aspect is the squared term in the first Friedmann equation, which allows the derivative of the scale factor to be either positive or negative. In other words, the universe can be either expanding or contracting (Friedmann's equations do not prohibit this possibility).

We can also identify the cosmological constant as an energy density

$$\rho_\Lambda = \frac{c^2}{8\pi G}\Lambda, \quad (1.16)$$

and it's very important to notice that the dark energy density remains constant.

Thanks to Hubble's studies and numerous observations, we now know that the universe is expanding. Within these equations, we can introduce another important parameter using equation (1.4)

$$\rho_{crit} = \frac{3H^2(t)}{8\pi G}, \quad (1.17)$$

this is the critical density (also called  $\rho_c$  in this thesis), which allows us to define the density parameter  $\Omega$  as follows

$$\Omega = \frac{\rho}{\rho_{crit}}. \quad (1.18)$$

which is particularly useful as it establishes a direct relationship between the density of the universe and its geometry. As previously discussed, there are three possible cases:

- If  $k = -1$ , then  $\Omega < 1$  and  $\rho < \rho_{crit}$ .  
In this case, the universe has negative curvature and follows a hyperbolic geometry (similar to a saddle shape).
- If  $k = 0$ , then  $\Omega = 1$  and  $\rho = \rho_{crit}$ .  
In this scenario, the universe is flat.
- If  $k = +1$ , then  $\Omega > 1$  and  $\rho > \rho_{crit}$ .  
Here, the universe has positive curvature and is closed with a spherical geometry.

As before, we want to rewrite the Friedmann equation introducing  $\Omega$ .

The Friedmann equation (1.15) became

$$\frac{H^2}{H_0^2} = \frac{\rho_m}{\rho_{crit,0}} + \frac{\rho_r}{\rho_{crit,0}} + \frac{\Lambda}{\rho_{crit,0}} = \Omega_m + \Omega_r + \Omega_\Lambda, \quad (1.19)$$

the left side term is equal to one because it's calculated at present time and  $\rho_{crit,0}$  is the critical density calculated at present time.

With this notation the relation between the three parameters is obviously given by  $\Omega(t) = \Omega_m(t) + \Omega_r(t) + \Omega_\Lambda(t)$  and  $\Omega_k$  associated at the curvature is  $\Omega_k(t) = -\frac{k}{H(t)^2 a^2} = 1 - \Omega(t)$ . Thanks to these relations we can rewrite the first Friedmann equation:

$$H^2(t) = H_0^2[\Omega_m(1+z)^3 + \Omega_r(1+z)^4 + \Omega_\Lambda + (1-\Omega)(1+z)^2]. \quad (1.20)$$

It has been said before that the solution of the covariant derivative of the stress-energy tensor depends on a parameter  $w$ . An analytical solution for the

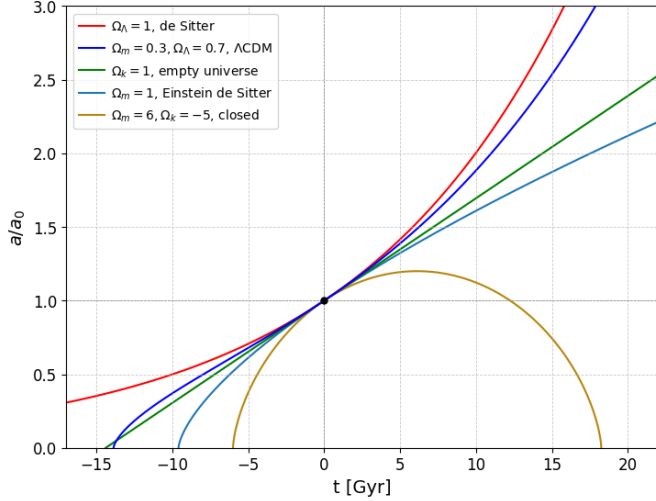


Figure 1.1: Evolution of the scale factor as a function of time in different type of universe. Credits [33].

scale factor can be derived by assuming that only one of the components with equation of state dominates the energy density.

In the early universe, after the Big Bang, the radiation contribution is more important than the contribution of matter and this is also called the radiation dominated era. In this epoch the density falling down very quickly:  $\rho(a) \propto a^{-4}$ . The radiation density has decreased enough to allow it to take over to matter, ushering in the matter dominated era where the density scale with the following trend:  $\rho(a) \propto a^{-3}$ .

So, immediately after the explosion, the universe entered a radiation-dominated era, during which it expanded slowly ( $\propto t^{1/2}$ ) while the density decreased rapidly. As the universe expanded, the gas cooled, leading to the matter-dominated era. In this era, according to the Friedmann equations, the expansion occurred at a faster rate ( $\propto t^{3/2}$ ), while the matter density decreased more slowly.

Recently we entered in the dark energy (DE) era where the DE is responsible for the expansion of the universe as we can easily see in fig. 1.2 in the lower right part.

## 1.3 Perturbations and their evolution

### 1.3.1 Linear perturbation

After the Big Bang, the universe underwent an early phase dominated by radiation, during which density fluctuations could not grow significantly due to the strong

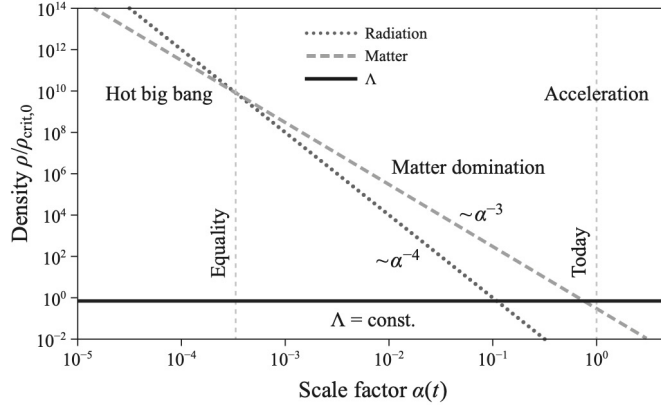


Figure 1.2: Evolution of cosmic components (radiation, matter and dark energy). The vertical lines mark the different eras. Fig. 5.2 in ref. [16].

radiation pressure. As the universe expanded and cooled, it transitioned to a matter-dominated phase, allowing these primordial fluctuations to start growing under gravity.

Around redshift  $z \sim 1100$  (ref. [16]), during the epoch of recombination, the universe became transparent to radiation: photons decoupled from matter and the cosmic microwave background (CMB) was released. The CMB provides a snapshot of the universe at that time, and its tiny temperature anisotropies (of the order of  $\mu\text{K}$ , see fig. 1.3) reflect the initial density perturbations in the primordial plasma. In fact, if the cosmological principle were perfectly respected and the distribution of matter and energy in the universe were really isotropic and uniform, the cosmic structures we currently observe would not exist.

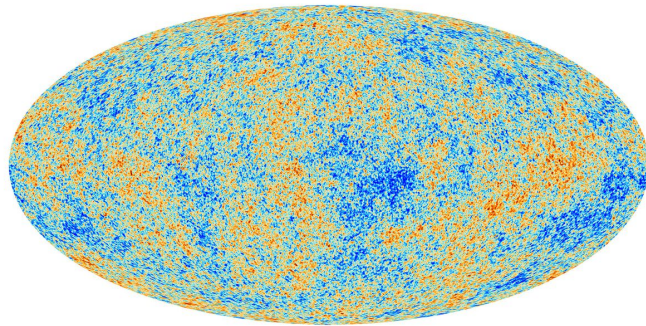


Figure 1.3: Temperature anisotropies in the cosmic microwave background. This image is based on data from the Planck release, published in 2013. Credits [26].

In a universe governed by non-relativistic matter, perturbations grow over time. Areas with a higher density of matter attract other matter, while regions with lower densities "empty" themselves. This is called gravitational instability and it is a crucial concept for understanding the processes that explain the formation of cosmic structures. However, the expansion of the universe damps the growth of these perturbations, preventing exponential growth and reducing the efficiency of gravitational collapse. The structure we observe today is assumed to have grown from small initial density perturbations in the density field due to the action of gravity. If the perturbations (shown in fig. 1.3) are very small, about  $\frac{\delta T}{T} \sim \frac{\delta\rho}{\rho} \sim 10^{-5}$ , as mentioned earlier, we can consider the contents of the universe as a perfect fluid characterized by pressure  $p(\vec{x}, t)$  and density  $\rho(\vec{x}, t)$ . Assuming a non-relativistic fluid, the evolution of the fluid is described by the continuity equation

$$\frac{D\rho}{dt} + \rho \nabla \cdot \vec{u} = 0.{}^1 \quad (1.21)$$

The perturbation of  $\rho(\vec{x}, t)$  can be written as  $\delta\rho(\vec{x}, t) = \rho(\vec{x}, t) - \bar{\rho}(t)$  (deviation from mean density) where  $\bar{\rho}(t)$  is the density background.

We can still write the density  $\rho(\vec{x}, t)$  in this epoch of the universe as  $\rho(\vec{x}, t) = \bar{\rho}(t)(1 - \delta(\vec{x}, t))$ .

Other necessary equation is the Euler's equation

$$\frac{D\vec{u}}{dt} = -\frac{1}{\rho} \nabla p - \nabla \Phi, \quad (1.22)$$

where  $\Phi$  is the gravitational potential associated with the Poisson equation

$$\nabla^2 \Phi = 4\pi G \rho. \quad (1.23)$$

One last equation is needed to close the system: the equation of state, which links pressure to density.

In particular, if the evolution of perturbation is adiabatic,  $p(\rho, S)$  is equal to zero for dark matter and  $p(\rho, S) \neq 0$  for baryonic matter and/or radiation.

The evolution of linear perturbations is governed by the combination of the previous equation that results in the following:

$$\ddot{\delta}_k + 2H\dot{\delta}_k + \delta_k \left[ \frac{k^2 v_s^2}{a^2} - 4\pi G \bar{\rho} \right] = 0, \quad (1.24)$$

where  $v_s$  is the sound speed in the fluid and  $a$  is the scale factor. This equation describes the evolution of perturbations in the early universe in the linear regime.

---

<sup>1</sup>Where  $\frac{D}{dt}$  indicate the convective derivative define as  $\frac{D}{dt} = \frac{\partial}{\partial t} + \vec{v} \cdot \nabla$ .

We now move to Fourier space to solve the differential equations:

$$\delta_{\vec{k}}(t) = \left(\frac{1}{2\pi}\right)^3 \int \delta(\vec{y}, t) e^{-i\vec{k} \cdot \vec{y}} d^3y, \quad (1.25)$$

where  $\vec{k} = \frac{2\pi}{\lambda}$ .

A particular scale exists, called the Jeans scale, which corresponds to the point where the term in brackets vanishes

$$K_J = a \sqrt{\frac{4\pi G \bar{\rho}}{v_s^2}}. \quad (1.26)$$

This marks a transition regime. For scales smaller than the Jeans scale (i.e.,  $k > K_J$ ), pressure dominates; for  $k < K_J$ , gravity dominates and perturbations begin to grow. Initially, the Jeans scale is very large, and all small perturbations cannot grow because pressure would erase them. After the reionization era<sup>2</sup>, the Jeans scale drops quickly and perturbations can grow. Another important aspect that we have to consider is the free-streaming damping: particles with high velocity can move from regions with high density to regions with small density and vice-versa. This effect calms the disturbances. If there are particles moving freely in the universe, it doesn't mean they will necessarily come together under the force of gravity. This is a scale called free-streaming scale, which is the distance that a dark matter particle can travel in a certain amount of time. Below this scale, even dark matter perturbations cannot grow because the particles move in a way that prevents them from clustering. This minimum scale depends on the mass of dark matter particles.

According to observation, we can see that small structures formed first, with dark matter halo having a mass of about  $10^6 M_\odot$ . This is very important because it tells us that particles with a very small mass, like neutrinos, cannot make up dark matter. They would produce much larger structures and would have a much higher free-streaming scale. This suggests that dark matter particles must be very massive and move slowly; this is what we call cold dark matter.

These structures grow in a hierarchical way. Baryons particles fall into the gravitational potential of dark matter if the structures are dense enough. As they fall, the density and pressure increase, which also raises the temperature. In this condition, the first stars begin to form. As we have seen before, radiation density decreases very quickly ( $\rho \propto a^{-4}$ ) while matter density decreases much more slowly ( $\rho \propto a^{-3}$ ). At a certain point, we reach the so-called matter-radiation equality, when the density of matter equals the density of radiation

$$\Omega_m(1+z)^3 = \Omega_r(1+z)^4, \quad (1.27)$$

---

<sup>2</sup>In cosmology, the era of reionization is the period following the big bang during which the mass of hydrogen that filled the universe became transparent to electromagnetic radiation.

where  $z$  is called the redshift of equality, with a value of approximately  $z \sim 3400$  (see fig. 1.2) according to ref [16]. From this moment, the universe entered the matter dominated era. In the linear regime, the solution for the perturbation in Fourier space can be rewritten as:

$$\delta_{\vec{k}}(t) = \delta_{\vec{k}_{\text{in}}} D(t), \quad (1.28)$$

where the first term depends only on  $\vec{k}$  (these are the initial perturbations observed in the cosmic microwave background), and the second term is called the linear growth factor ( $D(t)$ ). The latter has two possible solutions <sup>3</sup>:

$$\begin{aligned} D_-(t) &\propto H(t) \propto t^{-1}, \\ D_+(t) &\propto H(t) \int_0^t \frac{dt'}{a^2(t')H^2(t')} \propto t^{\frac{2}{3}}. \end{aligned} \quad (1.29)$$

Therefore, perturbations do not grow linearly in time; their growth is somewhat slower. It is important to note that even if the universe were not expanding, and even if dark matter had no pressure, not all structures could form. Only structures above a certain mass scale can form because the free streaming of the dark matter still resists gravitational collapse.

### 1.3.2 Relativistic perturbation

The relativistic theory of cosmological perturbations provides the most general and rigorous framework for studying the evolution of inhomogeneities in the Universe. Derived directly from general relativity, it overcomes the limitations of the Newtonian approximation and is valid across all scales and cosmic epochs. This formalism allows for a consistent treatment of scalar, vector, and tensor perturbations. In particular, the scalar perturbations, which are the most relevant for structure formation, are often analyzed in the conformal Newtonian gauge. This gauge simplifies the metric perturbation expressions by introducing two scalar potentials,  $\phi$  and  $\psi$ , directly related to the Newtonian gravitational potential and spatial curvature perturbation.

It's possible to construct this formalism by introducing a perturbed metric tensor:

$$g_{\mu\nu} = \bar{g}_{\mu\nu} + \delta g_{\mu\nu}, \quad (1.30)$$

where  $\delta g_{\mu\nu}$  is the perturbation that can be written as the sum of several contributions:  $\delta g_{\mu\nu}^S$ ,  $\delta g_{\mu\nu}^V$ , and  $\delta g_{\mu\nu}^T$  thanks to the decomposition theorem<sup>4</sup>. Here, the

<sup>3</sup>Assuming a universe with  $k = 0$  and matter dominated.

<sup>4</sup>In the first-order perturbation theory the scalar, vector and tensor part do not couple to each other according to ref. [12].

superscripts indicate respectively the scalar, the vector, and the tensor perturbation.

In order to simplify the problem, we can consider only the first scalar perturbation that can be written in terms of two potentials:  $\phi$  and  $\psi$ . In a suitable gauge, called a conformal Newton gauge, it is possible to define two gauge-invariant potentials, also called Bardeen potentials, with the following identities:

$$\begin{cases} \Phi = \phi, \\ \Psi = \psi. \end{cases} \quad (1.31)$$

This leads to a particularly simple writing for the perturbative matrix we are studying

$$\delta g_{\mu\nu} = \begin{pmatrix} -2\frac{\Phi}{c^2} & 0 \\ 0 & -2\frac{\Psi}{c^2}\delta_{ij} \end{pmatrix}. \quad (1.32)$$

Now the distance can be written in the following way

$$ds^2 = g_{\mu\nu}dx^\mu dx^\nu = a^2(t) \left[ -\left(1 + 2\frac{\Phi}{c^2}\right)c^2dt^2 + \left(1 - 2\frac{\Psi}{c^2}\right)\delta_{ij}dx^i dx^j \right], \quad (1.33)$$

and rewritten in comoving spherical coordinates

$$ds^2 = a^2(t) \left[ -\left(1 + \frac{2\Phi}{c^2}\right)c^2dt^2 + \left(1 - \frac{2\Psi}{c^2}\right)(d\chi^2 + f_k^2(\chi)d\Omega^2) \right], \quad (1.34)$$

where  $f_k(\chi)$  can assume three different forms

$$f_k(\chi) = \begin{cases} \sin(\chi) & \text{if } k > 0 \text{ (closed universe)} \\ \chi & \text{if } k = 0 \text{ (flat universe)} \\ \sinh(\chi) & \text{if } k < 0 \text{ (open universe)} \end{cases} \quad (1.35)$$

This perturbed metric is commonly used to describe astrophysical structures such as galaxy clusters. Although these systems are strongly non-linear in terms of matter overdensities (with density contrasts  $\delta \gg 1$ ), the gravitational potential  $\Phi$  remains small compared to  $c^2$  (typically  $\Phi/c^2 \sim 10^{-5}$ ), which justifies the use of linear perturbation theory for the metric. The matter density perturbations are connected to the potentials through the Poisson equation (1.23), which comes from the "00" component of the perturbed Einstein equations. Within the standard  $\Lambda$ CDM framework and assuming General Relativity with a perfect fluid, the two Bardeen potentials coincide:  $\Phi = \Psi$ . However, in more general theories of gravity or models with anisotropic stress, this equality can be violated. Therefore, detecting  $\Phi \neq \Psi$  may provide evidence for physics beyond the  $\Lambda$ CDM model, such as modified gravity or exotic interactions within the dark sector.

### 1.3.3 Non linear perturbation

Linear perturbation theory is a good approximation only when  $\delta\rho \ll 1$ . Unfortunately, actual observations suggest that structures have formed under non-linear conditions. This forces us to investigate non-linear evolution further, which requires more complex tools. On small scales it's possible to observe the nonlinear collapse of overdensity; this requires more complex tools to be described. This can be thought of as an overdense region that expands with the universe until it decelerates, reverses its motion, gravitationally collapses, and finally reaches virial equilibrium. However, to understand the formation of clusters on small scales, the main approach is numerical simulation. These simulations can be complicated as desired by adding dark energy, baryonic matter (e.g. gas), black holes, and supernovae. However, a simpler method is to consider only dark matter. This is still a very good approximation since it allows us to study dark matter halos in which galaxies form. The most used technique to study these problems is the simulation N-body. One of the famous N-body simulations is the millennium simulation that traced over 10 billion particles in a cube with sides approximately 2 billion light years long.

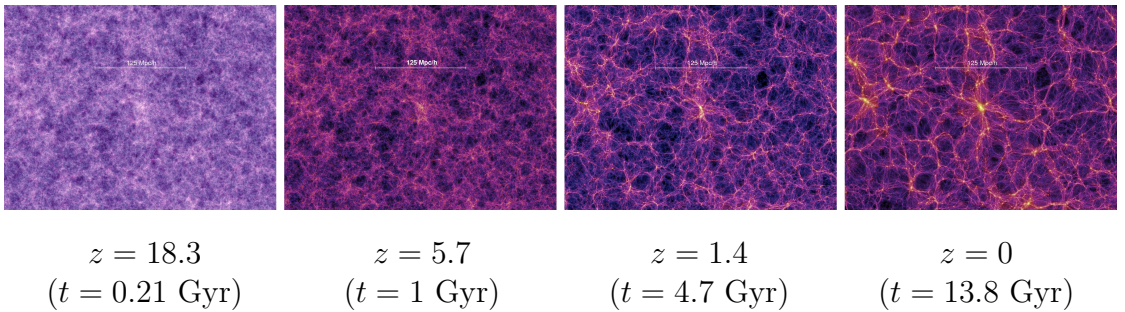


Figure 1.4: Evolution of the universe's large-scale structure as simulated in the Millennium Simulation Project, shown at different redshifts ( $z$ ). Each panel displays the distribution of dark matter on cosmological scales at a different redshift/time. Credits [77].

Of course, this is not the only way; another approximation used is the Zel'dovich approximation or the spherical collapse model or even the Lagrange perturbation theory. However, these, as mentioned above, are complex models that will not be addressed in this thesis.

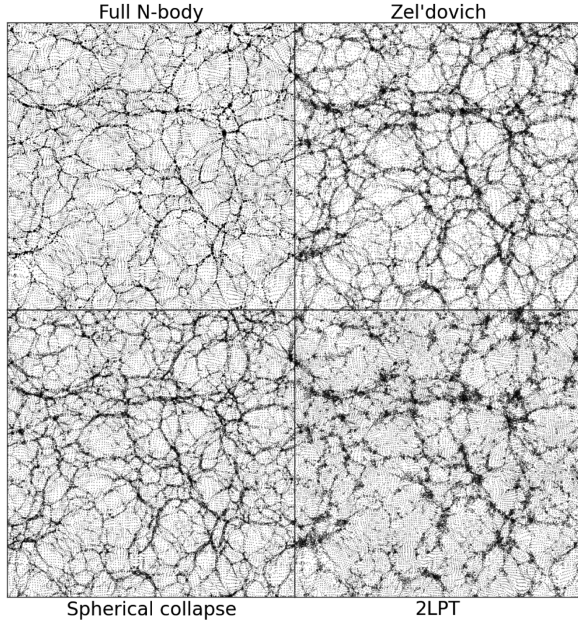


Figure 1.5: Top left is an N-body simulation, top right is in Zel'dovich approximation, bottom left is a simulation in spherical collapse approximation and the last bottom right frame is in lagrangian perturbation theory. Figure 10 in ref. [55].

## 1.4 Summary of $\Lambda$ CDM model

The  $\Lambda$ CDM model (Lambda Cold Dark Matter) is the current standard model of cosmology, providing a remarkably successful description of the Universe's evolution and composition. It assumes a flat universe (ref. [17]) composed of ordinary (baryonic) matter, cold dark matter (CDM), and a cosmological constant  $\Lambda$  accounting for dark energy.

According to recent observations, the  $\Lambda$ CDM model describes a universe composed of approximately 31% matter and 69% dark energy. More precisely, the density parameters are measured to be  $\Omega_m = 0.3111 \pm 0.0056$  and  $\Omega_\Lambda = 0.6889 \pm 0.0056$ , where  $\Omega_m$  includes both baryonic and dark matter (DM) components (ref. [1]). These values are derived from observations of the Cosmic Microwave Background (CMB), particularly from the Planck 2020 results (ref. [1]). While the addition of the cosmological constant is strictly necessary to explain the expansion of the universe (ref. [66]), the requirement for cold dark matter ensures the formation of large structures on cosmological scales that other types of dark matter couldn't explain. Indeed, other types of dark matter, which will be discussed in more detail in Chapter 2, fail to correctly explain the formation of large-scale cosmic structures. Dark matter is supported by a wide range of observational evidences across differ-

ent scales. On galactic scales, the flat rotation curves of spiral galaxies suggest the presence of extended dark matter halos (ref. [69]). On the scale of galaxy clusters, gravitational lensing and velocity dispersion measurements indicate a significant amount of unseen mass (ref. [14]). Finally, on cosmological scales, dark matter is essential to explain the pattern of the CMB anisotropies and the growth of large-scale structures (ref. [1], [76]). Another crucial parameter in the  $\Lambda$ CDM framework is the Hubble constant  $H_0$ , which quantifies the current rate of expansion of the universe. The value inferred from CMB data is  $H_0 = (67.66 \pm 0.42) \text{ km s}^{-1} \text{ Mpc}^{-1}$  (ref. [1]). However, this measurement is in tension with values obtained through local observations, such as the study of Type Ia supernovae; in fact, recent analyses report a significantly higher value:  $H_0 = 75.7_{-5.5}^{+8.1} \text{ km s}^{-1} \text{ Mpc}^{-1}$  (ref. [59]). This discrepancy, known as the Hubble tension, represents one of the most intriguing open problems in modern cosmology (see fig. 1.6 below).

Another important and recent study also observed discrepancies in dark energy, proposing that it is not truly constant (ref. [21]). All these tensions suggest that our current understanding of the universe — as described by the standard  $\Lambda$ CDM model — might be incomplete and motivates further investigation into the nature of dark matter, dark energy and possibly new physics beyond the standard model of cosmology. In fact, the  $\Lambda$ CDM model still fails to provide a natural explanation for the existence and physical origin of the cosmological constant.

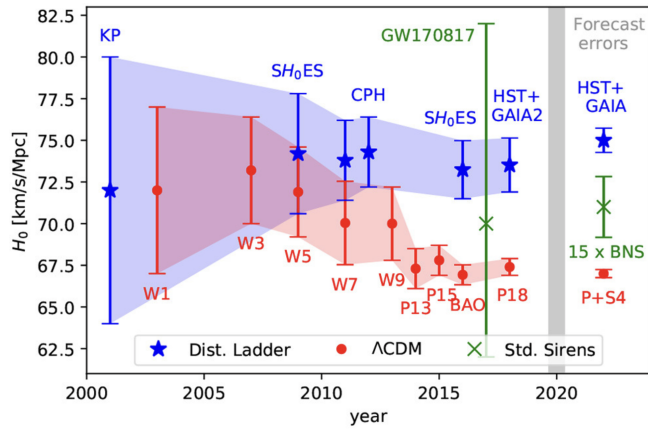


Figure 1.6: The data in blue represents the measurements made with the Cepheids, those in red refer to the data obtained with the CMB and finally the green lines are the results of gravitational wave observations. Figure 8 in ref. [29].

In particular, dark matter, which makes up the majority of the matter component in the universe, remains one of the least understood elements in the  $\Lambda$ CDM model. Although it works well on large scales and explains many observations, the model has several problems on smaller scales. These include the cusp-core prob-

lem, where the predicted steep density profiles in galaxy centers are not observed, and the missing satellite problem, where the simulations predict a larger number of small satellite galaxies are being detected (see Chapter 2).

These and other small-scale problems suggest that dark matter might not be entirely cold and collisionless as assumed in the standard cosmological model, but could instead possess self-interactions or exhibit different clustering behavior. Studying these tensions could thus provide crucial insights into the fundamental nature of dark matter.

For these reasons, in the following chapters, I will focus on the properties and distribution of dark matter, presenting more recent modeling approaches.



# Chapter 2

## Dark Matter Properties

As anticipated in the previous chapter, only about 31% of the universe is composed of matter, and a mere 5% of this is ordinary (baryonic) matter. This leaves a significant portion of the cosmos which composition and behavior cannot be explained by visible matter alone. In this chapter, we will focus on the first experimental evidence of the existence of dark matter proposed by Zwicky in ref. [85] and Vera Rubin in ref. [69].

There are many models used to describe the distribution of dark matter density profiles, like the Einasto profile, the Burkert profile (ref. [6]) and, for us in this thesis, the most used, the Navarro-Frenk-White profile (ref. [53]). Following, we will briefly explain the cusp-core problem (ref. [20]), the missing satellite problem (ref. [49]) and some possible solutions. Finally, we will discuss the nature of dark matter as well as its interactions with baryonic matter and dark matter itself (ref. [65]).

### 2.1 Experimental Evidence for the Existence of Dark Matter

#### 2.1.1 First Evidence by Zwicky

One of the earliest pieces of evidence for the existence of dark matter comes from Fritz Zwicky's 1933 observations of the Coma galaxy cluster (ref. [85]). This cluster is composed of approximately 800 galaxies, each with an estimated mass of about  $10^9 M_\odot$ .

The gravitational potential energy can be expressed as

$$\langle U \rangle = - \int_0^R \frac{GM(r)}{r} dm, \quad (2.1)$$

where  $M(r)$  is the mass enclosed within radius  $r$ . Assuming a uniform mass distribution, we can write:

$$M(r) = \frac{4}{3}\pi r^3 \rho \quad \Rightarrow \quad dm = 4\pi r^2 \rho dr, \quad (2.2)$$

with  $\rho$  representing the average density of the cluster. Substituting into eq. (2.1), we obtain:

$$\langle U \rangle = - \int_0^R \frac{G \cdot \left(\frac{4}{3}\pi r^3 \rho\right)}{r} \cdot 4\pi r^2 \rho dr = -\frac{3}{5} \frac{GM_{\text{tot}}^2}{R}, \quad (2.3)$$

where the total mass is

$$M_{\text{tot}} = \frac{4}{3}\pi R^3 \rho. \quad (2.4)$$

Next, applying the virial theorem,  $2\langle K \rangle + \langle U \rangle = 0$ , we express the average kinetic energy as:

$$\langle K \rangle = \frac{1}{2} M_{\text{tot}} \sigma_v^2, \quad (2.5)$$

where  $\sigma_v$  is the velocity dispersion. Replacing the theoretical value of mass ( $800 \cdot 10^9 M_\odot$ ) and solving for  $\sigma_v$ , we obtain:

$$\sigma_v = \frac{3}{5} \sqrt{\frac{GM_{\text{tot}}}{R}} \approx 80 \text{ km s}^{-1}. \quad (2.6)$$

However, Zwicky observed a much larger value of around  $1000 \text{ km s}^{-1}$  (ref. [85]), significantly higher than the predicted result. Assuming the velocity dispersion measurement is correct, the total mass of the cluster must be much greater than initially estimated:

$$M_{\text{tot}} = \frac{5}{3} \frac{R}{G} \sigma_v^2 \approx 1.25 \cdot 10^{14} M_\odot. \quad (2.7)$$

### 2.1.2 Rotation Curves

Another strong piece of evidence comes from the study of galactic rotation curves, first systematically measured by Vera Rubin (ref. [69]). According to Newtonian dynamics and General Relativity, the rotational velocity of stars in a galaxy should decrease with increasing distance from the galactic center. However, observations reveal that these velocities tend to remain approximately constant (see fig. 2.4). We can assume that most of the mass of a galaxy is contained in the central part called bulge (or central bulk). Consequently, we can imagine that there is a maximum in the rotation profile almost close to the center.

As a first approximation, we model the galaxy as having a constant density  $\rho_0$  up to a characteristic radius  $R_*$ , beyond which the density drops abruptly to zero.

This corresponds to a simplified top-hat density profile. Under this assumption, the total mass enclosed within a radius  $R < R_*$  is given by:

$$M(r < R) = \int_0^R \rho(r) d^3x = 4\pi\rho_0 \int_0^R r^2 dr = \frac{4}{3}\pi\rho_0 R^3, \quad (2.8)$$

meanwhile for radii greater than  $R_*$ , since the density is zero by construction, the enclosed mass remains constant

$$M(r > R_*) = \frac{4}{3}\pi\rho_0 R_*^3. \quad (2.9)$$

Then, we can calculate the velocity by balancing gravitational and centrifugal forces

$$v_c = \sqrt{\frac{GM(r)}{R}}, \quad (2.10)$$

that gives us two different results:

$$v_c(R) \sim \begin{cases} R & \text{for } R < R_*, \\ R^{-\frac{1}{2}} & \text{for } R > R_*. \end{cases} \quad (2.11)$$

This prediction implies that the rotation speed increases linearly in the central region (where mass grows with  $R^3$ ), and then falls off at larger radii (since no additional mass is enclosed beyond  $R_*$ ). However, this theoretical profile does not match observations: rotation curves of spiral galaxies tend to flatten out at larger radii rather than decline like we can see in fig. 2.4 below.

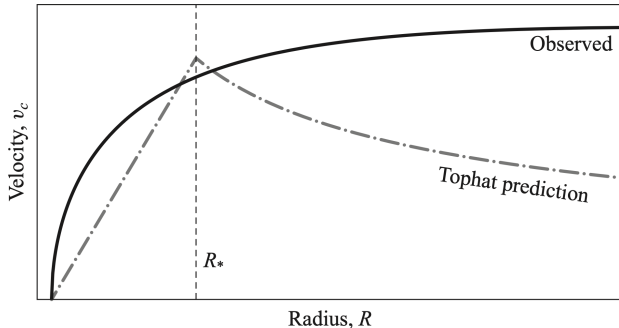


Figure 2.1: Rotation curve of a galaxy. The dotted line represents the theoretical prediction, while the solid black line shows the observed curve. Figure 3.5 in ref. [16].

Another important demonstration of the existence of dark matter is the anisotropies in the CMB (fluctuation power spectrum); this contains much information to determine the parameters of the standard cosmological model. In particular, as we

said in Chapter 1, before the recombination era, the universe was a dense plasma where baryons and photons were coupled. This fluid had small oscillations called baryonic acoustic oscillations (BAO), waves of pressure that propagated in the plasma. The velocity of these perturbations is the sound speed in this fluid, indicated by  $c_s^2$ .

BAO remains as a footprint in the CMB spectrum. In figure 2.2 below, the power spectrum of the CMB is shown. Green dots are data points with their error bars; at high and low multipoles, the model is well fitted by baryons and cold dark matter, while only in a very small region is it fitted by baryons only.

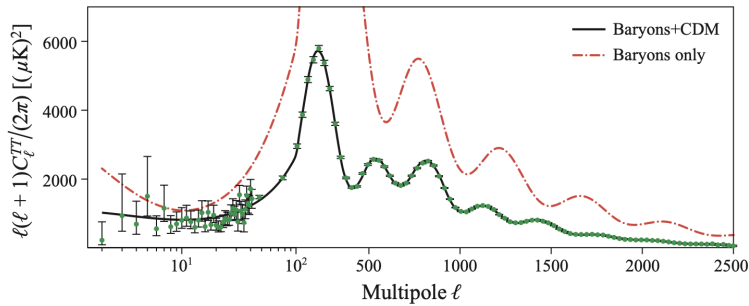


Figure 2.2: CMB power spectrum. On the  $x$ -axis the multipoles are reported and, on the  $y$ -axis, the amplitude of acoustic oscillations are reported. Figure 6.5 in ref. [16].

All these discrepancies indicate a significant amount of mass is present beyond the visible component — leading to the hypothesis of dark matter halos surrounding galaxies.

Over the decades, many hypotheses have been proposed to explain the nature of dark matter and, more generally, the missing mass. These include:

- Warm, hot and cold dark matter
- MACHOs (Massive Compact Halo Objects)
- WIMPs (Weakly Interacting Massive Particles)
- Modified Gravity Theories

MACHOs are "composed" by very compact objects like black holes, neutron stars and white dwarfs. However, none of these can explain the nature of dark matter because neutron stars and white dwarfs emit electromagnetic radiation, while the number of black holes necessary to explain the entire missing mass would be too high. Furthermore, from a statistical point of view, some stars would accrete

onto them and emit electromagnetic radiation (ref. [44]).

WIMPs are hypothetical particles  $\chi$  with a rest mass  $m_\chi$  in the range of 1–10 GeV (ref. [41]). These particles interact very weakly with Standard Model particles. In the early Universe, it was hot enough to produce  $\chi$  and  $\bar{\chi}$  in thermal equilibrium, but when the temperature fell below  $T \sim m_\chi$ , annihilation reactions could no longer maintain that equilibrium. Under this temperature, the abundance froze out.

A typical weak scale annihilation cross section  $\langle\sigma v\rangle \sim 10^{-26} \text{ cm}^3 \text{ s}^{-1}$  naturally yields the observed dark matter relic density; this is the so-called “WIMP miracle” (ref. [16]).

Modified gravity theories include several theoretical models that attempt to modify gravity by potentially extending General Relativity; for example there are tensor-scalar theories that include  $f(R)$  gravity, Brans-Dicke theory, Degenerate Higher-Order Scalar-Tensor (DHOST) or tensor-vector-scalar theories like MOND (Modified Newtonian Dynamics).

However, not all modified gravity models are designed to explain dark matter, in fact, MOND its relativistic extension were explicitly developed as alternatives to dark matter, aiming to reproduce galactic rotation curves without invoking unseen mass (ref. [47]).

$f(R)$  gravity try to include the effects of dark matter and dark energy into the curvature of space-time (ref. [9]) while Brans-Dicke and DHOST theories focus their attention on dark energy (ref. [40]).

In the rest of the chapter, as previously mentioned, we will focus on dark matter models.

## 2.2 Navarro-Frenk-White Dark Matter Density Profile

In order to investigate the role of dark matter and its properties, we introduce the Navarro-Frenk-White (NFW), a universal model for fitting the slope of dark halos proposed by Julio Navarro, Carlos Frenk e Simon White during 1996 (ref. [52], [53]) after simulations of dark matter. An important feature of this model is its universality: the NFW profile successfully describes dark matter halos across a wide range of masses and redshifts, making it a robust and widely adopted tool in cosmology, as demonstrated in ref. [53]. The Navarro-Frenk-White analytical form is the following:

$$\rho(r) = \rho_c(z) \frac{\delta_c}{\frac{r}{r_s} \left(1 + \frac{r}{r_s}\right)^2}. \quad (2.12)$$

Here  $\delta_c$  is a characteristic dimensionless density,  $r_s$  is the scale radius and  $\rho_c(z)$  the critical density at time  $z$ . Physically,  $r_s$  is the radius that indicates where the profile becomes steeper.

From a mathematical point of view  $r_s = r_{-2}$ , where  $r_{-2}$  denotes the radius at which the derivative of the logarithm of the density is equal to  $-2$ .

The radial profile is proportional to  $r^{-1}$  at small radii and  $r^{-3}$  at large radii.

As we can see in the following figure 2.3, the uniformly good fits across all masses and cosmologies provide clear evidence for the universality of the NFW profile, even in different cosmologies.

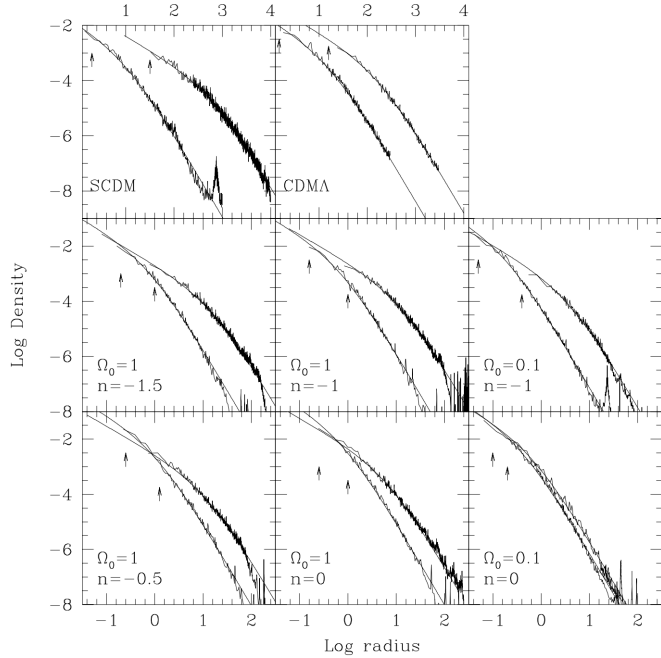


Figure 2.3: Density profile of two dark matter haloes, the left-hand curve in each panel represent the low mass halo and the right-hand curve the massive halo. The thick jagged lines in each panel are the data obtain from simulation while the thin smooth curves are the two-parameter NFW fits. Credits [53].

It is also useful to introduce additional quantities and physical relationships, such as  $r_{200}$ ,  $M_{200}$  and the concentration  $c = \frac{r_{200}}{r_s}$  (sometimes indicated with  $c_{200}$ ). The radius  $r_{200}$  is defined as the radius within which the average density is 200 times the critical density of the Universe. The corresponding mass  $M_{200}$  is calculated as:

$$M_{200} = \frac{100H^2(z)r_{200}^3}{G}, \quad (2.13)$$

but remembering that the critical density is  $\rho_c(z) = \frac{3H^2(z)}{8\pi G}$  and combining these

two equations it's possible to find

$$M_{200} = \frac{4}{3}\pi r_{200}^3 \cdot 200\rho_c. \quad (2.14)$$

The characteristic density is related to the concentration  $c$  through the following formula (ref. [53])

$$\delta_c = \frac{200}{3} \frac{c^3}{[\ln(1+c) - c/(1+c)]}, \quad (2.15)$$

then, this one can be expressed as:

$$\rho_s = \rho_c(z) \cdot \delta_c = \frac{M_{200}}{4\pi r_s^3 [\ln(1+c) - c/(1+c)]}. \quad (2.16)$$

This model provides a mass density profile for galaxy clusters and their dark matter halos. However, there are some differences between simulations and observations. For example, the Navarro-Frenk-White model is affected by the so-called cusp problem, according to which the dark matter density profile is expected to rise steeply toward a peak near the central region—where most of the matter is concentrated—and then drop off rapidly. However, this trend is not observed experimentally. Due to this singularity, it's also possible to define the generalized Navarro-Frenk-White (see e.g. ref. [83]), also called gNFW hereafter, introducing  $\gamma$ :

$$\rho(r) = \frac{\rho_s}{\left(\frac{r}{r_s}\right)^\gamma \left(1 + \frac{r}{r_s}\right)^{3-\gamma}}, \quad (2.17)$$

where  $0 < \gamma < 2$  (note that by setting  $\gamma = 1$ , we obtain the standard Navarro-Frenk-White density profile) and  $\rho_s$  is the scale density defined as follows

$$\rho_s = \left(\frac{r_{200}}{r_s}\right)^{\gamma-3} \frac{M_{200}(3-\gamma)}{4\pi r_s^3 {}_2F_1\left(3-\gamma, 3-\gamma; 4-\gamma; -\frac{r_{200}}{r_s}\right)}, \quad (2.18)$$

where  ${}_2F_1$  is an hypergeometric function.

In this model, an arbitrary law shaped the central cusp with  $r^{-\gamma}$  while, out of the central region, it falls off as  $r^{-3}$  (ref. [83]).

Inside a galaxy cluster, most of the mass is contained in the dark halo and offers us a perfect natural laboratory to test and study dark matter models.

Due to the strong dependence of  $\rho(r)$  on the nature of dark matter, determining the value of  $\gamma$  is a crucial step in improving our understanding of dark matter. In particular, values of  $\gamma < 1$  may indicate the presence of fuzzy, decaying, or self-interacting dark matter, while higher values ( $\gamma > 1$ ) can result from mass accretion processes, as discussed in ref. [4].

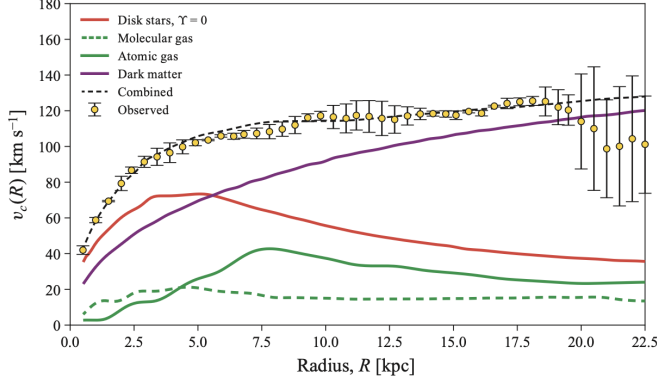


Figure 2.4: According to the figure 3.7 in ref. [16] this is the best fit with the NFW model for the rotational curve of M33 (Triangulum Galaxy).

There are also several dark matter profiles such as the Einasto profile or Burkert profile whose mathematical expressions are, respectively, the following:

$$\rho(r) = \rho_s \exp \left\{ -2m \left[ \left( \frac{r}{r_s} \right)^{\frac{1}{m}} - 1 \right] \right\} \quad \rho(r) = \frac{\rho_s}{\left( 1 + \frac{r}{r_s} \right) \left[ 1 + \left( \frac{r}{r_s} \right)^2 \right]} \quad (2.19)$$

with  $m \in \mathbb{N}$  in the Einasto profile. While the NFW model exhibits a cusp, diverging at small radii, the Einasto and Burkert profiles flatten to a constant value for  $r \rightarrow 0$ .

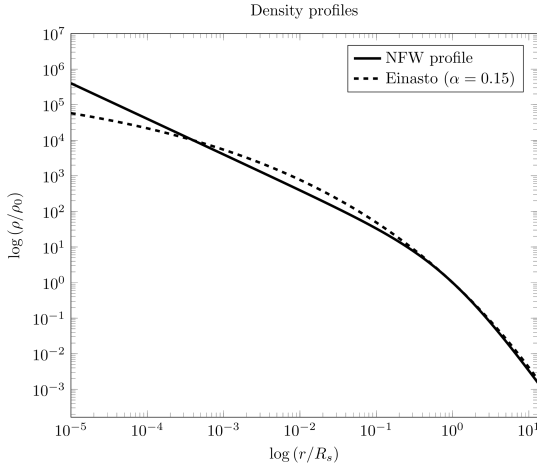


Figure 2.5: Comparison between NFW and Einasto profiles in log scale. Credits [82].

## 2.3 Cusp-core problem

The cusp-core problem (also called the CC problem) is that some galactic rotation curves are better described by models that do not have a cusp, such as the isothermal density profile. This is in contrast to the N-body simulation which, like the NFW model, predicts the formation of a cusp profile. The first attempts to solve the CC problem involved looking for statistical errors with observation or simulation limits. Other possible explanations include the baryonic effect (gas and stars for example) in the dark matter profile or cosmological solutions that change the  $\Lambda$ CDM model according to ref. [20].

### 2.3.1 Baryonic solution

The baryonic solution includes three possible effects: Supernovae Feedback Flattening (SNFF), Dynamical Friction from Baryonic Clumps (DFBC) and Mass-dependent density profiles.

The SNFF mechanism is very similar to AGN feedback, with the difference that the latter only occurs if the galaxy has an active black hole at its center, while SNFF can also occur in smaller galaxies. For this reason, we will focus on SNFF. In the first one, supernovae explosions transfer energy to gas that change the gravitational potential. This perturbation is "sensed" by dark matter expanding its distribution, forming a core. This mechanism works better in small galaxies (dwarf galaxies). However, a single supernova is not enough. For this model to be valid, repeated supernova explosions are needed. Instead, the baryonic clumps fall toward the center of the gravitational potential and transfer energy due to friction with the dark matter. This leads to a redistribution of dark matter that flattens the cusp.

Another criticism of the SNFF model is the need for too high a star formation rate. So only for  $M > 10^6 M_\odot$  there is a good approximation between the stellar mass and the profile slope.

The physical mechanism of DFBC can be divided into several phases: the linear phase where proto-galactic structures composed of dark matter and refusals of gas are formed. In the second phase, dark matter gravitationally collapses, forming potential wells that attract baryonic matter. The falling unstable gas fragments into dense clumps of gas, forming disks. When the surface density of the disk exceeds a critical threshold, the disk becomes particularly unstable and fragments into clumps in Jeans equilibrium capable of reaching considerable dimensions and masses. A small part of the gas in the clumps forms stars. Due to dynamical friction, energy and angular momentum are transferred to the dark matter. This process compensates for the adiabatic contraction of the dark matter. At this point (with a redshift  $z \sim 2$ ) the SNFF model can be resumed, which destroys

the smaller clumps. This model works fine within  $M < 10^6 M_\odot$  where SNFF fails. The main problem with this model is the presence of bulges or swellings, which are in fact capable of reforming the cusps.

Last baryonic solution is the mass-dependent density profiles. Using another form of generalized NFW (gNFW) written as follows (ref. [20]):

$$\rho(r) = \frac{\rho_s}{\left(\frac{r}{r_s}\right)^\gamma \left[1 + \left(\frac{r}{r_s}\right)^\alpha\right]^{(\beta-\gamma)/\alpha}}, \quad (2.20)$$

where

$$\begin{aligned} \alpha &= 2.94 - \log_{10} [(10X + 2.33)^{-1.08} + (10X + 2.33)^{2.29}] \\ \beta &= 4.23 + 1.34X + 0.26X^2 \\ \gamma &= -0.06 + \log_{10} [(10X + 2.56)^{-0.68} + (10X + 2.56)], \end{aligned} \quad (2.21)$$

and  $X = \frac{M_*}{M_{\text{halo}}}$ .<sup>1</sup>

The idea is to make this profile dependent on a specific mass ratio  $X$ . The physical meaning of the parameters is as follows:  $\gamma$  indicates the internal slope,  $\beta$  indicates the external slope, and  $\alpha$  indicates the transition between the internal and external zone. With this dependence by mass of halo, simulation (conducted with stellar and gas mass) can fit the density profile to find the best value for these three parameters in function of mass.

### 2.3.2 Cosmological solution

On the contrary, cosmological solutions propose to radically modify the standard cosmological model. To do this, a different type of dark matter is proposed: Warm Dark Matter (WDM) and Self Interacting Dark Matter (SIDM).

#### Warm Dark Matter

The warm dark matter is a deviation from the standard cold dark matter used in the  $\Lambda$ CDM model. Due to the decrease in speed, in function of time, DM should be more important in the past, dampening the formation of structure on small scales. This is very similar to the dynamical friction from baryonic clumps that heat the dark matter. Thanks to higher velocity, the density profile is flattened. However, also WDM is not a perfect solution; in order to produce sufficiently large cores ( $\sim 1$  kpc) and alleviate the cusp-core problem, Warm Dark Matter would require a very low particle mass ( $\sim 0.1$  keV). However, such a low mass is incompatible with

---

<sup>1</sup>Note that with  $(\alpha, \beta, \gamma) = (1, 3, 1)$  we obtain again the NFW.

the formation of large-scale structures, which instead demand higher masses ( $\sim 1\text{--}2$  keV). On the other hand, WDM particles with masses in that range produce only very small cores ( $\sim 10\text{--}20$  pc), which are too small to solve the cusp-core problem. Therefore, a single WDM particle mass cannot simultaneously account for both the observed cored density profiles in dwarf galaxies and the successful formation of large-scale structure, highlighting a fundamental tension within the WDM scenario.

### Self Interacting Dark Matter

The last type of dark matter proposed is self-interacting dark matter (SIDM), analyzed in ref. [65]. In this alternative model, dark matter particles interact not only through gravity but also through collisions. This is in contrast with the  $\Lambda$ CDM framework, which treats dark matter as perfectly collisionless. This type of dark matter was proposed to resolve and mitigate some discrepancies between astrophysical observations and  $\Lambda$ CDM simulations.

However, this kind of matter is not relativistic, which is why it is very different from the warm dark matter that we discussed earlier. While SIDM is still consistent with observations on large scales, many differences appear on small scales (clusters and substructures), where collisions between dark matter particles can modify the distribution of mass (ref. [75]). This contribution on the smallest scales is the key to understanding why SIDM could resolve the cusp-core problem. Self-interaction can flatten the density profile in the core region because collisions between particles distribute energy outwards, forming a blunt core. There is another problem that SIDM can explain: many simulations show subhalos much less dense than those observed, with a gravitational lensing signal much smaller than that observed experimentally. In the SIDM model, it is possible to form a core collapse after an initial phase of formation. When halos are initially very concentrated, the interactions can increase the concentration and density; furthermore, the densities can even exceed those predicted by the  $\Lambda$ CDM model. Thanks to this phenomenon, also described in the literature, SIDM is capable of describing some excess compactness observed in certain cluster substructures compared to standard  $\Lambda$ CDM simulations.

The interaction cross section identifies the probability of collision between two particles. In the  $\Lambda$ CDM model, this value is almost zero, but this is not the case in the SIDM model; in particular, from galaxy clusters, it is possible to find an upper limit  $\sigma/m \sim 0.19 \text{ cm}^2/\text{g}$  (ref. [24]). A value so small indicates a very weak interaction, contradicting what has been said so far. To solve this, many models introduce a velocity-dependent cross section. In other words, collisions between

dark matter particles are frequent in systems with low relative velocities (dwarf galaxies) and rare in systems with high relative velocities (clusters).

In particular, in ref. [65], two types of SIDM are well described: frequent SIDM (fSIDM) and rare SIDM (rSIDM). In the first one, interactions are more frequent with small angles of scattering between particles; in contrast, rSIDM describes rare, large, and isotropic scattering angles.

Simulations can be conducted in different regimes: only with DM (ODM) or with full physics (dark matter and baryonic matter), also called FP. In both cases, fSIDM and rSIDM produce density profiles with flattened cores, perfectly as expected by SIDM theory. However, in the FP regime, simulated clusters show a higher central density with respect to the collisionless case. This indicates that, with baryonic physics, the DM auto interaction increases the concentration of matter in the center.

Also the abundance of substructure in clusters is affected by changes; in fact, in DMO simulations, a strong suppression of the number of subhalos inside the cluster (probably destroyed by DM-DM collisions) is demonstrated in comparison to the collisionless model. However, when baryonic matter is included, this suppression is attenuated because self-interactions tend to push the DM outwards but stars and gas mitigate the overall mass loss and consequently the probability that the subhalo will be destroyed.

This is even more evident between rSIDM and fSIDM because: in rSIDM collisions are few but strong, this leaves more time for the halo to relax and the mass loss is moderate. In fSIDM collisions are frequent with small angle and the cumulative effect is very similar to a viscous brake that pushes away dark matter making the sub-halo deficit higher.

Although self-interacting dark matter appears to resolve many inconsistencies, there are still many unresolved questions. For example, it is very difficult to reconcile an interaction cross section that, on one hand, is high enough to solve the cusp-core problem, but on the other hand, must remain very weak. It is also difficult to perform these simulations by separating the contributions of self-interacting dark matter from those due to baryonic physics, because the latter can mask the phenomena we attribute to dark matter. Even current technology has limitations: algorithms would have to scale down to the mean free path of dark matter particles, and this represents a limit for our computing power.

## 2.4 Missing satellite problem

The missing satellite problem (or MSP) is another challenge. This problem concerns the discrepancy between the number of subhalos predicted by cosmological simulations (according to  $\Lambda$ CDM model approximately 100 satellites are planned for Milky Way in ref. [37]) of only dark matter and the satellite galaxies observed. In particular, observations detected many fewer satellites than expected from simulation in DM regime, for example, only 10 for our galaxy (e.g. ref. [37]). This leads us to better understand the role of baryonic matter inside galaxies. A hydrodynamical cosmological simulation was used in ref. [49], covering a simulated universe box of 51.7 Mpc and using dark matter particles with a mass of  $4.5 \cdot 10^5 M_\odot$ . In the simulation, galaxies similar to M83 were modeled, meaning galaxies with a baryonic mass approximately equal to that of M83. To do this, halos with masses between 0.6 and  $1 \cdot 10^{11} M_\odot$  were selected (M83 has a mass of about  $0.7 \cdot 10^{11} M_\odot$ ). Non-isolated galaxies were excluded, meaning galaxies with a massive neighbor within 700 kpc. This allowed the identification of 146 galaxies similar to M83 (M83 analogs). To compare them with observations, these galaxies were placed at the same distance as M83 (4.9 Mpc) and randomly distributed in the simulated sky. All subhalos (candidate satellites) within 330 kpc of projected distance and 350 kpc along the line of sight were collected. A central region was then excluded to simulate the area occupied by the main galaxy, where the high brightness makes it difficult to detect satellites. At this point, a satellite luminosity function can be built — in other words, the number of satellites in each luminosity bin. What was found is that 13 satellites of M83 are confirmed while of all 146 simulated analogues, 3 have no satellites brighter than  $M_V = -10$  ( $V$ -band absolute magnitude) and 2 have only one. Most have several, but in total fewer than those actually observed for M83. In conclusion, the tension at faint end ( $-14 \leq M_V \leq -12$ ) is  $> 3\sigma$ . So the discrepancy is particularly significant at low luminosities. These results indicate an opposite problem; there are too many satellites in M83, and this is a message that  $\Lambda$ CDM model doesn't estimate yet the abundances of dwarf galaxies.

Another possibility to explain the MSP is the interaction between dark matter and baryonic matter. Like we have seen in this chapter, many past models only use dark matter, but more recent studies have demonstrated that baryonic phenomena can drastically modify the surrounding environment. In fact, this is the main idea in ref. [5] where Milky Way satellites are studied; in particular, the role of feedback from supernovae and tidal interaction with the galactic disk. The issue arises when comparing the predicted properties (density) of these subhalos based on simulations to the observed properties of dwarf galaxies based on observations.

In the article, public catalog of subhalos of the Via Lactea II simulation is used, considering, for each subhalo, the maximum velocity at infall time  $v_{\text{infall}}$  (or, in other words, the maximum of the rotation curve before entering into the main halo), the mass into 1 kpc at  $z = 0$  indicated with  $M_{<1\text{kpc}}(z = 0)$  and the orbit. Due to the absence of baryonic matter in simulations, authors apply corrections to consider baryonic effects mentioned above<sup>2</sup>.

This correction is applied to all subhalos with  $v_{\text{infall}} < 50 \text{ km s}^{-1}$  (it is not applied to more massive, Magellanic-like subhalos). For low-mass subhalos with  $v_{\text{infall}} < 30 \text{ km s}^{-1}$ , the correction mimics gas loss due to UV heating/stripping and the enhanced tidal mass loss caused by the host's baryonic disk. For more massive subhalos with  $v_{\text{infall}} > 30 \text{ km s}^{-1}$ , the correction also accounts for the supernova-feedback-induced flattening of the central dark-matter profile, which makes these satellites more susceptible to tides.

When assessing complete disruption, we adopt two thresholds: for subhalos with  $v_{\text{infall}} > 30 \text{ km s}^{-1}$  we consider them destroyed if they have lost  $> 90\%$  of their mass and have pericentric passages within 20 kpc; for subhalos with  $v_{\text{infall}} < 30 \text{ km s}^{-1}$  we consider them fully stripped if they have lost  $> 97\%$  of their mass since infall.

In ref. [37], another type of solution is proposed. This time, the focus is on the observational completeness; in fact, only a small part of our galaxy is observed in a very detailed way. Introducing an observational completeness correction factor, defined as the integration of tridimensional density of all satellites over all virial volume divided by the volume really observed by the survey (ref. [39], [81]), the entire number of satellites deeply changes. The assumption of various profiles influences the correction. In a model with a more concentrated profile, such as NFW, corrections are smaller than those produced by strong tidal stripping due to the presence of a baryonic disk.

Thanks to this correction, we obtain a minimum number of satellites that matches the CDM predictions and, like other studies cited above, even poses the related problem known as the "too many satellites problem".

---

<sup>2</sup>Via Lactea II only consider dark matter simulations.

# Chapter 3

## Galaxy clusters

Most galaxies in the universe are grouped together in clusters of tens or hundreds of galaxies. Clusters typically contain 50 or more bright galaxies (ref. [48]). These objects are the most massive structures in the universe and represent the final point of the hierarchical formation of cosmological structures; in fact, their size is about 1 Mpc and a typical mass of  $10^{14} - 10^{15} M_{\odot}$ . Due to these dimensions, galaxy clusters are the meeting point between astrophysics and cosmology.

In this chapter, we are going to describe this complex structure in order to investigate the nature of dark matter and its interaction with the baryonic matter introducing techniques and equations used in Chapter 4.

### 3.1 Structure of galaxy clusters

Despite the number of galaxies hosted, the mass belonging to galaxies constitutes the smallest part. Within a galaxy cluster, the total mass is composed of several elements: the brightest cluster galaxy (BCG), the intra-cluster medium (ICM), the galaxy population, and finally dark matter (DM).

As we can easily see in fig. 3.1, galaxies are only a small part of the cluster. About 5% of the entire mass is formed by galaxies (ref. [35]), another 10% is formed by gas (ICM) and about 80% by dark matter.

#### 3.1.1 Intra Cluster Medium (ICM)

The Intracluster Medium (ICM) is hot, diffuse gas that permeates the space between the galaxies in the cluster itself (ref. [10], [31]). It constitutes the most important part of the baryonic matter, with an average abundance of 10%. Initially, it was thought that the presence of this gas could exclude the need to introduce dark matter, but even adding its contribution does not amount to the total mass

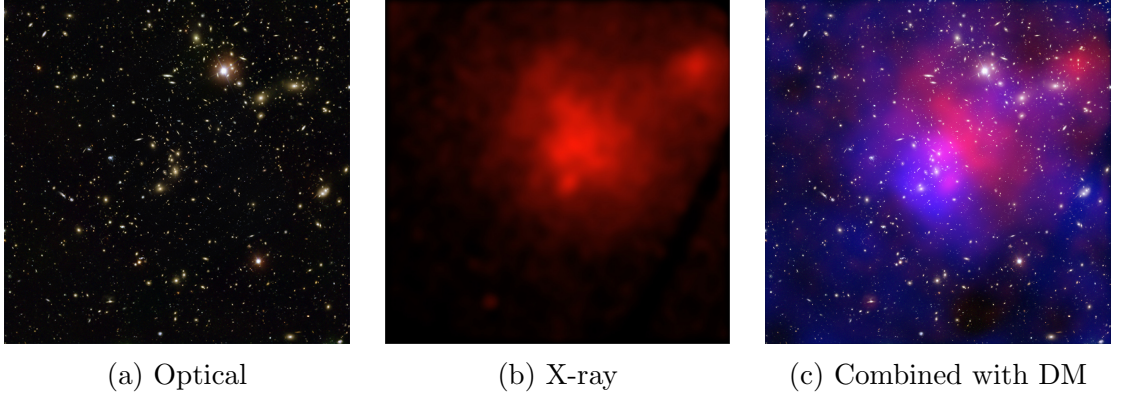


Figure 3.1: Multi-wavelength observations of the galaxy cluster Abell 2744. **Left:** Optical image taken by Hubble Space Telescope and VLT. **Center:** X-ray image by Chandra X-Ray Observatory. **Right:** Combined images, the blue zone is the distribution of dark matter according to Hubble's data. Credits [11].

of the cluster calculated through the virial theorem or the study of the X-ray radiation emitted by the ICM itself. Due to its high temperature ( $10^7 - 10^8 \text{ K}$ ), the ICM can be considered completely ionized. Its density is very low, about  $10^{-4} - 10^{-2} \text{ cm}^{-3}$ . It contains heavy elements like Carbon, Oxygen, and Iron. This composition indicates the presence of phenomena such as supernovae that generate and distribute these elements. Its emission on the electromagnetic spectrum is located in the X-ray region. It is generated by the interaction of free electrons (the ICM can be considered like an ionized plasma) and atomic nuclei with thermal bremsstrahlung.

The ICM is also responsible for the Sunyaev-Zel'dovich effect (or SZ effect), photons of CMB that are crossing the cluster interacting with ionized ICM through an inverse scattering Compton with free high-energy electrons, this phenomenon causes a distortion in the CMB (ref. [78]).

In a relaxed cluster, the radial distribution for gas may be described by the beta model:

$$n(r) = \rho_s \left[ 1 + \left( \frac{r}{r_c} \right)^2 \right]^{-\frac{3}{2}\beta}, \quad (3.1)$$

where  $\beta$  is an index that describes how the gas density decreases as a function of radius and  $r_c$  is the core radius. With  $\beta = 2/3 \sim 0.67$  we have the King profile (ref. [38]).

### 3.1.2 Brightest Cluster Galaxy (BCG)

In almost all galaxy clusters, there is a giant galaxy that dominates the cluster, typically a giant elliptic galaxy with an extended and diffused halo. This galaxy is also called Brightest Cluster Galaxy (BCG). These galaxies are very massive, with mass over  $10^{12} M_{\odot}$ , and also their contribution to the cluster luminosity is very important. Most of the time this galaxy is an elliptical cD galaxy (where "D" stands for "diffuse") as reported in ref. [48]. Due to this morphology, its surface brightness profile is well described by the Vaucouleurs profile (ref. [19]), a particular case of the Sersic profile (ref. [73]). However, this last one is very difficult to deproject, so we can use more simply the Jaffe luminosity profile (ref. [36])

$$L_J(r) = L_{source} \frac{r}{r_J} \left(1 + \frac{r}{r_J}\right)^{-1}, \quad (3.2)$$

assuming that the luminosity profile follows the mass profile it's possible to define a mass profile for the BCG as

$$M(r) = M_* \frac{r}{r_J} \left(1 + \frac{r}{r_J}\right)^{-1} = L_{source} X_L, \quad (3.3)$$

where  $X_L$  is the mass-luminosity ratio measured in  $M_{\odot}/L_{\odot}$ . This profile has a density profile written in the following way

$$\rho(r) = \frac{\rho_J}{\left(\frac{r}{r_J}\right)^2 \left(1 + \frac{r}{r_J}\right)^2}, \quad (3.4)$$

where  $r_J$  is Jaffe's radius and  $\rho_J = \frac{M_*}{4\pi r_J^3}$  with  $M_*$  the total stellar mass in the BCG. This profile will be used in Chapter 4 to fit the contribution to the mass cluster given by the BCG.

In dynamically relaxed systems, the BCG is usually located close to the center defined either by the X-ray peak of the intra cluster medium gas or by the mass peak reconstructed from gravitational lensing (ref. [25]).

However, recent X-ray/optical studies show that this is not universal: up to  $\sim 40\%$  of BCGs are displaced from the X-ray peak by tens of kiloparsecs, with a median separation of  $\sim 15$  kpc and extreme cases beyond 100 kpc (ref. [18]).

The origin of BCGs is still debated. Early studies proposed a single-process such as only the BCG cannibalism mechanism (ref. [58]) or only the cooling flows (ref. [15]), but more recent work indicates that BCGs are more likely to form through a multi-stage process. At high redshift, the bulk of the primary stellar mass is assembled in short, intense episodes of star formation and only later does the galaxy grow mainly through mergers with satellites that spiral toward the cluster center during its evolution.

### 3.1.3 Galaxies

Like we said before, galaxies form only about 5% of the entire mass of a galaxy cluster, but this is not a good reason to ignore them. In fact, galaxies can be used as tracers to determine the mass of the cluster itself through dynamical analyses (this is exactly what we will do in the next Chapter 4).

There are several types of galaxies that can be divided in few groups in function of their colors and morphology. From the morphological point of view, according to Hubble classification, galaxies have 3 principal shapes: elliptic, spiral and irregular. The age of a galaxy is connected to its color, as the presence of a large number of red stars indicates that the galaxy is old (red stars live more than blue stars); on the opposite, a large number of blue stars indicates a young galaxy.

Galaxies are also divided into two sequences defined by a number of characteristic properties. Early type galaxies are characterized by elliptical and lenticular shape, old and red stars, poor in gas, a low star formation rate (SFR). On the other hand, late type refers to spiral and irregular galaxies, with young and blue stars, rich in gas and active SFR.

It is important to note that in Hubble's scheme "early type" and "late type" are morphological labels, not age indicators. In the nearby Universe, early-type galaxies generally host older stellar populations and late-type galaxies younger ones, but the terms themselves do not encode age; they persist as a historical holdover from Hubble's original classification.

In galaxy clusters, the majority of member galaxies are early type systems. These galaxies are typically red, bulge dominated, massive and characterized by old stellar populations with little or no star formation. On the other hand, late type galaxies are bluer, disk dominated, gas rich, with a high star formation rate but they are a smaller fraction within clusters compared with the entire population. In particular, ref. [2] studied the galaxy population of the massive cluster MACS 1206 as a function of radius from the center of the cluster. What it is possible to find is that the shape of the star mass function (SMF hereafter) of SF galaxies is independent from the environment or clustercentric radius. Instead, the shape of the SMF of passive galaxies depends on the environment. In the core, massive passives dominate and light passives and SF are lacking; towards the outside, SF and low mass passives increase.

These general "properties" are well illustrated in figure 3.2.

In the end, the stellar mass density profile is significantly more concentrated than the number density.

In a relaxed cluster, galaxies are characterized by the distribution of cluster galaxy velocities and positions. The projected number density of galaxies typically follows the cluster's mass density distribution; highest in the central regions and

decreasing with cluster radius. Some observations show that the distribution can be described by an NFW profile with early-type galaxies more concentrated toward the center than late-type (ref. [4]). The radial velocity of individual galaxies is distributed around a mean in a Gaussian function (ref. [71]). In a first approximation, this distribution is usually adopted to simplify the problem, but many studies have demonstrated that this is a very good approximation consistent with observations<sup>1</sup> (ref. [84]). Anyway, the dispersion velocity in a cluster decreases from the center to the outer region.

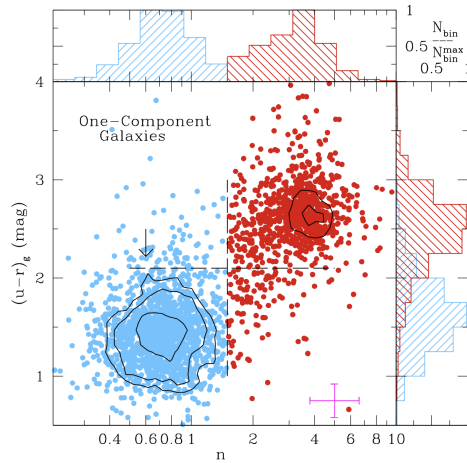


Figure 3.2: Figure shows the global-Sérsic index distribution. Two distinct peak clearly emerge: a red highly concentrated sequence populated by elliptical galaxies and a blue diffused sequence populated by disk systems. Disk only systems are represented by filled, blue circles and elliptical systems by filled, red circles. This bimodality reflects the fundamental separation between early type and late type galaxies. Credits [7].

## 3.2 Mass reconstruction

In Chapter 2, we have seen an application of the virial theorem to determine the mass of a galaxy. This is not the only possible method; other important and useful approaches include analyzing the light emitted by galaxies, studying their dynamical properties, or observing their distortion through gravitational lensing.

---

<sup>1</sup>This is true if the velocity is not too high.

### 3.2.1 Mass reconstruction from X-ray observations

We can imagine a galaxy cluster as a system of gas in hydrostatic equilibrium, within a spherical and symmetric environment at constant temperature. Under these hypothetical conditions, it is possible to determine the total mass <sup>2</sup> distribution in the cluster. The condition for hydrostatic equilibrium can be written as follows:

$$\frac{dp}{dr} = -\frac{GM(< R)\rho}{r^2}, \quad (3.5)$$

where  $\rho$  is the gas density,  $p$  is the pressure, and  $M(< R)$  is the mass contained within radius  $R$  in the cluster. Due to the high temperature of the gas, we can use the ideal gas law expressed in terms of density:

$$p = \frac{kT\rho}{\mu m_H}, \quad (3.6)$$

where  $k$  is the Boltzmann constant,  $\mu$  is the mean molecular weight of gas. We also assume that a large amount of gas is formed by hydrogen. Now we can differentiate (3.6) and equate it with the hydrostatic equilibrium condition (3.5) and find:

$$\frac{kT}{\mu m_H} \left( \frac{1}{\rho} \frac{d\rho}{dr} + \frac{1}{T} \frac{dT}{dr} \right) = -\frac{GM(< R)}{r^2}, \quad (3.7)$$

and from this find the mass

$$M(< R) = -\frac{kTr^2}{G\mu m_H} \left[ \frac{d\log \rho}{dr} + \frac{d\log T}{dr} \right]. \quad (3.8)$$

Where  $M(< R)$  is the cumulative mass within  $R$  radius. This is the result reported in ref. [30] and [62]. With this equation, if it is possible to measure the temperature of gas (for example, with an X-ray telescope) and the total visible mass, it's possible to find the total mass of the cluster and then the percentage of dark matter.

### 3.2.2 Mass reconstruction with lensing

In 1919, Arthur Eddington demonstrated the General Relativity theory through the deflection of the light of some stars following the passage of the latter in the gravitational field produced by the Sun (ref. [22]). A similar method can be applied to galaxy clusters, providing a wonderful way to study and calculate the mass contained in a galaxy. Light travels through empty space and it is deflected by the presence of massive objects such as galaxy clusters.

---

<sup>2</sup>Obviously, the mass is the combination of dark and baryonic matter.

In General Relativity, propagation of light subject to a gravitational potential  $\Phi$  can be described as in a medium with a refractive index

$$n \sim 1 - \frac{2\Phi}{c^2}. \quad (3.9)$$

The deflection angle is proportional to the transversal gradient of the index  $n$  that light meets during the path. Indicating with  $\vec{\alpha}$  the angle of deflection and with  $\nabla_{\perp} n$  the gradient of  $n$  perpendicular to the direction of propagation, we can write in general:

$$\vec{\alpha} = - \int \nabla_{\perp} n \, dl \approx \frac{2}{c^2} \int \nabla_{\perp} \Phi \, dl, \quad (3.10)$$

where the integral is along the way of the light ray through the gravitational field. The minus sign indicates that the deviation is toward the region with higher  $n$ , or deeper gravitational potential (ref. [50]). Now we can apply the upper formula (3.10) to calculate the deflection by a point mass  $M$ .

Let's consider a light ray which passes at a certain impact parameter  $\xi$  (minimum distance between the light ray and mass) from the mass  $M$  and let's set the  $z$ -axis as the direction of propagation of non-deflected light and  $\vec{\xi}$  a bidimensional vector on the perpendicular plane with respect to  $z$ -axis. In this case, with a point mass, the deflection angle is simply given by

$$\tilde{\alpha} = \frac{4GM}{c^2 \xi}, \quad (3.11)$$

where  $M$  is the mass of the deflector body,  $\xi$  is the impact parameter<sup>3</sup>. However, most of the time, mass is not a single dot but a continuous distribution of mass. In this case, we make a reasonable approximation: if the region where the mass is concentrated is much smaller than the distance between the source and the observer, we can imagine that the deflection essentially occurs in a single “layer” around the plane of the lens (see e.g. ref. [62]).

We then introduce a coordinate system on the plane of the lens, perpendicular to the line of sight and we denote with  $\Sigma(\vec{\xi})$  the surface mass density (or, in other words, the integrated mass along the line of sight at an arbitrary point  $\vec{\xi}$  of the lens plane).

The deflection angle can be rewritten in terms of position as follows

$$\vec{\alpha}(\vec{\xi}) = \frac{4G}{c^2} \int \frac{\Sigma(\vec{\xi}')(\vec{\xi} - \vec{\xi}')}{|\vec{\xi} - \vec{\xi}'|} d^2 \xi'. \quad (3.12)$$

To understand how the deflection of light, due to a large mass, is translated in alternate positions and shapes, it's important to analyze the geometry of the source-lens-observer system.

---

<sup>3</sup>See ref. [50] for more details.

Now let's consider a lighting source ( $S$ ) behind the lens ( $L$ ) as compared to an observer ( $O$ ).

In the absence of the lens, the observer can see the source with an angle  $\beta$  as

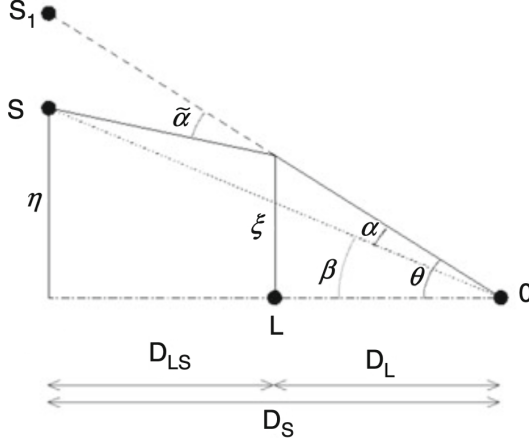


Figure 3.3: Scheme of gravitational lensing.  $S, S_1, L$  and  $O$  are respectively the real position of the source, the position of image of source from the view of the observer, the lens and the finally the observer.  $\xi$  is the impact parameter (minimum distance between deflected light ray and body that produce lens).  $\vec{\alpha}$  is the deflected angle and  $\vec{\alpha}$  the reduced deflected angle. In the end,  $D_{LS}$ ,  $D_L$  and  $D_S$  are respectively the distance of lens-source plane, distance lens-observer plane and distance source-observer plane. Credits [41].

compared to the optic axis lens-observer; in the presence of the lens, the light ray is deflected with an angle  $\vec{\alpha}$  reaching the observer with an effective angle  $\vec{\theta}$ . Now we can introduce the reduced angle  $\vec{\alpha}$  that can be written, with some geometry, as

$$\vec{\alpha} = \frac{D_{LS}}{D_S} \vec{\alpha}, \quad (3.13)$$

where  $D_{LS}$  is the projected distance between the lens and source, while  $D_S$  is the projected distance of the source from the observer. This reduced angle  $\vec{\alpha}$  represents the actual angular displacement of the source position as seen by the observer, taking into account that the deflection occurs at the plane of the lens and “projecting” this deflection up to the source plane. The fundamental equation of the gravitational lensing allows us to connect angles in the optic scheme below

$$\vec{\beta} = \vec{\theta} - \vec{\alpha}(\vec{\theta}).^4 \quad (3.14)$$

---

<sup>4</sup>This relation can be founded by  $\vec{\theta}D_S = \vec{\beta}D_S + \vec{\alpha}D_{LS}$  if corners are enough small.

Due to the dependence of the position of the objects, the deflection angle can be variable; for example, if  $\xi$  is smaller, the deflection will be bigger. It is also very important to notice that there are a few solutions for this equation, so it is possible to have more images for a single source.

We have defined  $\vec{\alpha}$  (3.13) and reduced angle (3.11) before, so combining all of them in the last one (3.14) we obtain

$$\vec{\beta} = \vec{\theta} - \frac{D_{LS}}{D_S} \vec{\alpha}. \quad (3.15)$$

For a lens with circular symmetry and mass given by fixed uniform surface density we can write  $M(\xi) = \Sigma\pi\xi^2$  (mass in a circle with radius  $\xi$ )

$$\alpha = \frac{D_{LS}}{D_S} \tilde{\alpha} = \frac{D_{LS}}{D_S} \frac{4\pi G \Sigma(\xi)}{\xi c^2}, \quad (3.16)$$

It is also possible to introduce a critical surface density

$$\Sigma_{crit} = \frac{D_S}{D_{LS} D_L} \frac{c^2}{4\pi G}. \quad (3.17)$$

Furthermore  $\xi = D_L \theta$  and substituting all into the lens equation, we found a linear formula

$$\beta = \theta - \frac{4\pi G \Sigma(\theta)}{c^2} \frac{D_L D_{LS}}{D_S} \theta. \quad (3.18)$$

A fascinating phenomenon happens when the source, lens and observer are aligned. In this case  $\beta = 0$  and the previous equation gives life to the Einstein ring (see fig. 3.5)

$$\theta_E = \sqrt{\frac{4GM(\theta_E)}{c^2} \frac{D_{LS}}{D_L D_S}}. \quad (3.19)$$

This is used to determine two kinds of regimes: strong lensing ( $\theta < \theta_E$ ) and weak lensing ( $\theta > \theta_E$ ).

### Weak lensing

The weak lensing regime occurs when the lens has a surface density lower than the critical one ( $\Sigma < \Sigma_{crit}$ ) over the entire field considered, so that no multiple images or very pronounced arches are formed.

Individual sources undergo changes too small to be distinguished from the intrinsic variability of galaxies' shapes and brightnesses. However, by statistically analyzing a large number of background sources, it is possible to reveal a consistent correlation in the distortions: typically, background galaxies tend to be stretched tangentially around the lens center with the semi-major axis of the image ellipse oriented perpendicular to the radius joining it to the lens center (ref. [16]). This phenomenon can be easily seen in an illustrative example in fig. 3.4.

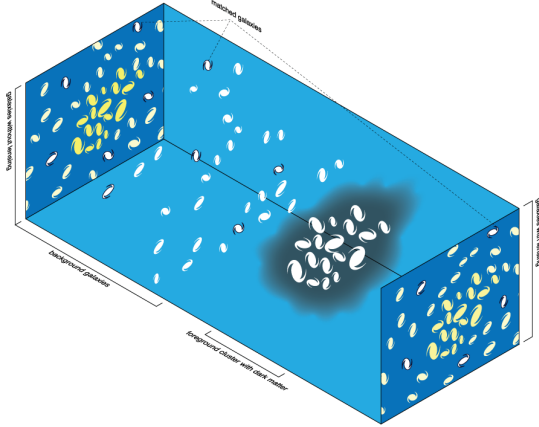


Figure 3.4: Three-dimensional representation of weak lensing: a foreground galaxy cluster weakly distorts the images of background galaxies along the line of sight. On the left, the same galaxies are shown without lensing; on the right, the lensed images appear slightly stretched and tangentially aligned around the cluster's mass. Credits [70].

### Strong lensing

When the effect of a lens is strong enough to produce multiple images or easily visible macroscopic distortions of a single background source. It normally occurs when the surface density is greater than the critical one ( $\Sigma > \Sigma_{crit}$ ).

If the alignment is almost perfect or if the source is very large, bright arches or even Einstein rings can form.

Sometimes, the magnification can be so strong to allow us to see objects too faint, this creating a giant natural gravitational space telescope giving us several data.

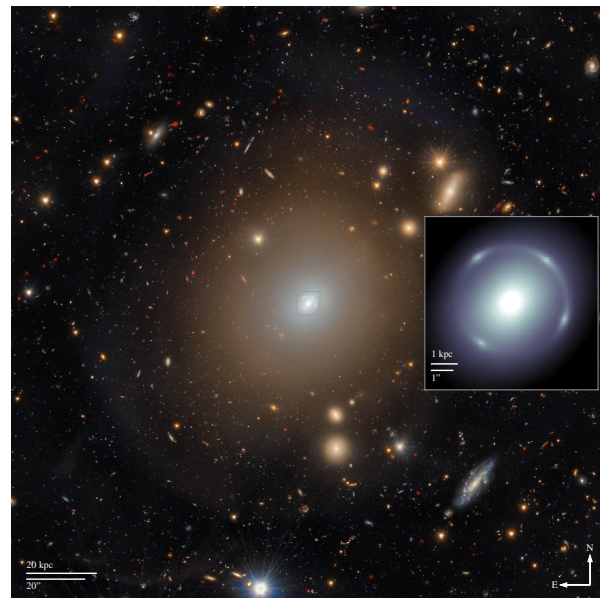


Figure 3.5: A wonderful example of strong lensing: Einstein ring around NGC 6505, photographed by the Euclid Space Telescope. The large background image shows the full cluster with the Einstein ring structure clearly visible. The inset panel (right-side) provides a close-up view of the ring. Figure 1 in ref. [56].

### 3.3 Mass reconstruction with kinematics of member galaxies

As seen in Chapter 2, it is possible to use the expressions for galaxy velocities to reconstruct the mass of a cluster. We will now introduce and explain some fundamental equations, like the Vlasov and Jeans equations, for the next chapter. Galaxy clusters are very different from gases, where particles collide with each other. In fact, here the predominant interaction is gravitational, which acts on large scales and which strength intensifies as galaxies approach each other. For this reason, it will be useful and sufficient to consider our system as a collection of collisionless particles.

#### 3.3.1 Vlasov equation

The Vlasov equation describes the evolution of a self-gravitating system of collisionless particles in terms of the distribution of particles in position-velocity phase space  $(\vec{x}, \vec{v})$ . Conceptually, it imposes the conservation of particle density in phase space along the motion; in absence of collisions, particles move so that the distribution, described by a function  $f(\vec{x}, \vec{v}, t)$ , remains constant along a phase trajectory. The flow of particles in phase space then behaves like an incompressible fluid as long as the interactions of the particles are negligible. For the purposes of discussion on galaxy clusters, this remains a very good approximation until relaxation times due to close encounters between particles are comparable with the age of the universe. A cluster can then be treated as a collisionless system in which the dynamics are governed by a gravitational potential generated by the mass distribution.

Now, with the distribution function  $f(\vec{x}, \vec{v}, t)$  we construct the number of particles in a volume element of the phase space.

$$dN = f(\vec{x}, \vec{v}, t) d^3x d^3v. \quad (3.20)$$

The time evolution of  $f$  is obtained by imposing continuity in phase space. Consider a six-component state vector (three related to position and three related to velocity).

$$w = (\vec{x}, \vec{v}), \quad (3.21)$$

its equation of motion will be

$$\dot{w} = (\dot{\vec{x}}, \dot{\vec{v}}) = (\vec{v}, -\nabla\Phi), \quad (3.22)$$

where  $\Phi$  is the gravitational potential that satisfies the usual Poisson equation. Putting everything together, phase-space continuity is written as the following

equation:

$$\frac{\partial f}{\partial t} + \sum_{i=1}^6 \frac{\partial(f\dot{w}_i)}{\partial w_i} = 0, \quad (3.23)$$

Now, since the gravitational potential does not explicitly depend on  $\vec{v}$  and that  $\vec{x}$  and  $\vec{v}$  are independent variables, it is possible to integrate the eq (??) and obtain the Vlasov equation

$$\frac{\partial f}{\partial t} + \sum_{j=1}^3 \left( v_j \frac{\partial f}{\partial x_j} - \frac{\partial \Phi}{\partial x_j} \frac{\partial f}{\partial v_j} \right) = 0, \quad (3.24)$$

or more conveniently written thanks to the convective derivative

$$\frac{Df(\vec{x}, \vec{v}, t)}{dt} = 0, \quad (3.25)$$

highlighting that the derivative of  $f$  along the motion is zero and that consequently the density of the particles (equivalently to the incompressible fluid) is conserved.

### 3.3.2 Jeans equation

The Jeans equation is obtained as the moment of the Vlasov equation and allows us to connect dynamical observable properties such as mean velocity, dispersion velocities and their anisotropies with gravitational potential. From a certain point of view, the Jeans equation is analogous to the Euler equation for a self-gravitating fluid where the pressure is replaced by the dispersion of velocities.

Defines itself the spatial density of particles  $\nu(\vec{x}, t)$  and the mean velocity  $\bar{v}_i(\vec{x}, t)$  as

$$\nu(\vec{x}, t) = \int f(\vec{x}, \vec{v}, t) d^3v \quad \bar{v}_i(\vec{x}, t) = \frac{1}{\nu} \int v_i f(\vec{x}, \vec{v}, t) d^3v, \quad (3.26)$$

and, manipulating eq. (3.24), it is possible to obtain

$$\frac{\partial \nu}{\partial t} + \frac{\partial(\nu \bar{v}_i)}{\partial x_i} = 0, \quad (3.27)$$

which is the continuity equation for numerical density  $\nu(\vec{x}, t)$ . This equation represents the conservation of the number of galaxies in a given volume and the temporal variation of  $\nu$  is due to the transport of particles (galaxies in our case) through the boundaries of the volume. The momentum of the Vlasov equation is obtained by multiplying by  $v_j$  and integrating again in the space of velocities; in this way we obtain a balance equation of the momentum quantities for a collisionless system

$$\frac{\partial(\nu \bar{v}_j)}{\partial t} + \frac{\partial(\nu \bar{v}_i \bar{v}_j)}{\partial x_i} + \nu \frac{\partial \Phi}{\partial x_j} = 0, \quad (3.28)$$

where  $\overline{v_i v_j}$  is given by

$$\overline{v_i v_j} = \frac{1}{\nu} \int v_i v_j f d^3 v. \quad (3.29)$$

Now the equation (3.28) can be manipulated; multiplying the continuity equation by  $\overline{v_j}$ , then we subtract from the equation (3.28) and finally, using the Leibniz rule<sup>5</sup>, we also introduce the velocity stress tensor  $\sigma_{ij}^2$  defined as:

$$\nu \sigma_{ij}^2 = \nu (\overline{v_i v_j} - \bar{v}_i \bar{v}_j) = \nu [\overline{v_i v_j} - \bar{v}_i \bar{v}_j]. \quad (3.30)$$

We thus obtain the final form of the equation we are looking for, thus finding the Jeans equation. From a physical point of view, the Jeans equation relates observable dynamical quantities with gravitational potential

$$\nu \frac{\partial \bar{v}_j}{\partial t} + \nu \bar{v}_i \frac{\partial \bar{v}_j}{\partial x_i} = -\nu \frac{\partial \Phi}{\partial x_j} - \frac{\partial (\nu \sigma_{ij}^2)}{\partial x_i}. \quad (3.31)$$

It is analogous to the Euler equation for a fluid. In the left side we have the time variation of momentum of the system and its derivative in space. In the right side, term  $-\partial(\nu \sigma_{ij}^2)/\partial x_i$  plays the role of a pressure gradient. The term  $-\nu \partial \Phi / \partial x_j$  is instead the gravitational force (for mass unit) that tends to accelerate particles towards regions of lower potential, that is, towards higher mass concentrations. Since the clusters are considered in spherical symmetry approximation and in dynamical equilibrium, it is convenient to project the Jeans equation along the radial direction by setting the center of the cluster as the origin and thus rewrite the Jeans equation in spherical coordinates

$$\frac{d(\nu \sigma_r^2)}{dr} + \frac{\nu(r)}{r} [2\sigma_r^2(r) - \sigma_\theta^2(r) - \sigma_\phi^2(r)] = -\nu(r) \frac{d\Phi}{dr}, \quad (3.32)$$

where  $\sigma_r$  is the velocity dispersion along the radial direction,  $\sigma_\theta$  is the velocity dispersion along the angular direction  $\theta$  and  $\sigma_\phi$  is the dispersion along the angular component  $\phi$ . The velocity dispersion profile is given by

$$\beta(r) = 1 - \frac{\sigma_\theta^2 + \sigma_\phi^2}{2\sigma_r^2}. \quad (3.33)$$

Obviously, if we are in spherical approximation, the dispersions along the tangential and altazimuth directions are equal,  $\sigma_\theta = \sigma_\phi$ . The equation (3.33) is thus reduced to the following

$$\beta(r) = 1 - \frac{\sigma_\theta^2}{\sigma_r^2}. \quad (3.34)$$

---

<sup>5</sup>See ref. [68] for more details on calculus.

Sign and amplitude of  $\beta$  indicated whether the orbits are preferably radial or tangential. Setting the dispersion of radial velocities equal to the tangential one ( $\sigma_r = \sigma_\theta$ ) we will have  $\beta = 0$ , this leads to isotropic orbits (the radial and tangential directions are equivalent). As the radial tendency increases ( $\sigma_r > \sigma_\theta$ ),  $\beta \rightarrow 1$  thus arriving at the limit of purely radial orbits. When tangential orbits are favored instead ( $\sigma_\theta > \sigma_r$ ),  $\beta$  decreases. In the extreme limit we have ideal circular orbits with  $\sigma_r \rightarrow 0$  and  $\beta \rightarrow -\infty$ .

Introducing  $\beta(r)$  into spherical Jeans equation (3.32), this can be rewritten as:

$$\frac{d[\nu(r)\sigma_r^2(r)]}{dr} + 2\beta(r)\frac{\nu(r)\sigma_r^2(r)}{r} = -\nu(r)\frac{d\Phi(r)}{dr}. \quad (3.35)$$

This equation relates the gradient of the gravitational potential to the radial variation of velocities and to the anisotropy term. In this way, if we measure through observations the density profile  $\nu(r)$  of the galaxies in the cluster, the dispersion of radial velocities  $\sigma_r(r)$  and anisotropy  $\beta(r)$ , it is possible to determine the gravitational potential  $\Phi(r)$  by solving the Jeans equation and, from this, obtain the mass density profile of the cluster.

## 3.4 CLASH and the CLASH–VLT program

The Cluster Lensing And Supernova survey with Hubble (CLASH) is a 524-orbit multi-cycle treasury program that observed 25 massive galaxy clusters thanks to the Hubble Space Telescope between 2010 and 2013 to determine their mass profiles through gravitational lensing (ref. [64], [74]). Using 16 broadband filters from the near-UV to the near-IR on the Wide Field Camera 3 (WFC3) installed during Servicing Mission 4 in May 2009 on the Hubble Space Telescope (ref. [51]) and on the Advanced Camera for Surveys (ACS), CLASH reaches four primary goals:

1. map the dark matter distribution in galaxy clusters through strong and weak gravitational lensing;
2. detect Type Ia supernovae out to  $z \sim 2$  to measure the role of dark energy;
3. discover highly magnified galaxies at  $z > 7$ ;
4. study the structure and evolution of cluster galaxies.

To complement the Hubble survey with spectroscopic redshifts, the CLASH–VLT Large Program carried out an extensive campaign with the VIMOS spectrograph on ESO’s Very Large Telescope (VLT). The survey targeted 13 CLASH clusters at  $0.2 < z < 0.6$ , obtaining about 31 000 spectra, with typically 500-1000 cluster members and  $\sim 200$  lensed background galaxies for each system (ref. [67],

[13]). These data provide the velocity, necessary for joint lensing–dynamical mass reconstructions.

In the end, to obtain high definition data of the BCG, the integral field spectrograph MUSE (Multi Unit Spectroscopic Explorer) on the VLT was used, collecting a total of 25 exposures of 1800 s each in April-May 2015 and April 2016. The three-pointing mosaic covers an effective area of  $2.63 \text{ arcmin}^2$ ; owing to the overlap between pointings, the central  $\sim 0.5 \text{ arcmin}^2$  reaches a depth of  $\sim 8.5 \text{ h}$ , while the remaining area integrates for  $\sim 4 \text{ h}$  (ref. [8]).

### 3.4.1 MACS 1206

MACS 1206 (or, more precisely, MACS J1206.2-0847) is a galaxy cluster located to  $z = 0.4398$  with J2000 coordinates RA  $12^{\text{h}}06^{\text{m}}12.15^{\text{s}}$  and DEC  $-8^{\circ} 48'3.4''$ <sup>6</sup> discovered in the MAssive Cluster Survey (MACS) as reported in ref. [23] and its mass is well determined with gravitational lensing and Chandra X-ray emission (ref. [79]). This cluster was deeply studied during the CLASH-VLT campaign using the Hubble Space Telescope and VIMOS as previously mentioned. In order to obtain more precise data for the central region, the spectrograph MUSE was utilized to explore in detail the BCG. MACS 1206 can be considered as an overall dynamically relaxed system, with an almost round projected matter distribution (see ref. [34]). Based on the CLUMPS algorithm developed in ref. [3], 468 cluster members are identified within 2.16 Mpc. For the choice of the cluster center, the BCG center was taken as a reference (ref. [60]).

The dispersion velocity for the BCG is obtained with the method described in ref. [72] and the surface brightness profile is fitted with a Jaffe profile. The luminosity in the  $I$ -band is  $L_{BCG} = 4.92 \cdot 10^{11} L_{\odot}$  and a Jaffe radius equals 39 kpc (ref. [60]). The mass of the ICM instead is taken from [28] and [4]. Finally, the stellar mass of member galaxies used in the next chapter for the analysis is taken from ref. [2]. This cluster will be examined in detail in the next chapter due to its physical properties and makes MACS 1206 a perfect object to test our theories and simulation code.

---

<sup>6</sup>Where RA and DEC indicate Right Ascension and Declination respectively refered to the center of cluster.



Figure 3.6: Galaxy cluster MACS J1206.2 photographed by Hubble Space Telescope. Credits [27].

Parameter	Value	Units
$z$ (redshift)	0.439	–
$M_{200}$	$1.4 \times 10^{15}$	$M_\odot$
$r_{200}$	1.98	Mpc
Gas temperature $T$	10.5	keV
$\beta$ (profile)	0.67	–
$r_c$ (core radius)	174.2	kpc

Table 3.1: Principal parameters about cluster MACS 1206



# Chapter 4

## Analysis with MG-MAMPOSSt code

Modify Gravity – Modelling Anisotropy and Mass Profiles of Observed Spherical Systems<sup>1</sup> (or MG-MAMPOSSt hereafter) is a program that derives the mass profile of galaxy clusters from the analysis of the kinematics of galaxies with the hypothesis that the system has spherical symmetry and dynamical relaxation. It's the evolution of the previous method MAMPOSSt (ref. [43]), able to work in standard gravity as well as in many non-standard scenarios including popular dark energy/modified gravity frameworks (see ref. [61]).

The code explores the projected phase space composed of the projected position of the galaxy and velocity along the line of sight indicated with  $v_z$  and called l.o.s. hereafter. These speeds refer to the cluster rest frame.

To determine the velocities along the line of sight, redshift data, which in turn are obtained from spectroscopic analyses, is used as described in the end of the previous chapter. The velocities are assumed to be distributed according to a Gaussian. MG-MAMPOSSt also attributes a parametric profile characterized by velocity anisotropy, gravitational potential, mass profile and number density profile. Then, Jeans's equation (3.35), under the assumption of dynamic equilibrium and spherical symmetry, is resolved and likelihoods are computed over a multidimensional grid of values. In order to do this, the code uses a Monte Carlo Markov Chain (or MCMC) which is particularly useful for a large number of parameters or a large number of haloes.

MG-MAMPOSSt can use different types of priors: flat and Gaussian. Flat priors can be used in case you do not want to privilege any particular value within a given range. Conversely, a Gaussian prior is a prior that assumes that the param-

---

<sup>1</sup>In this thesis we are not interested with modify gravity, so the code is used under General Relativity regime.

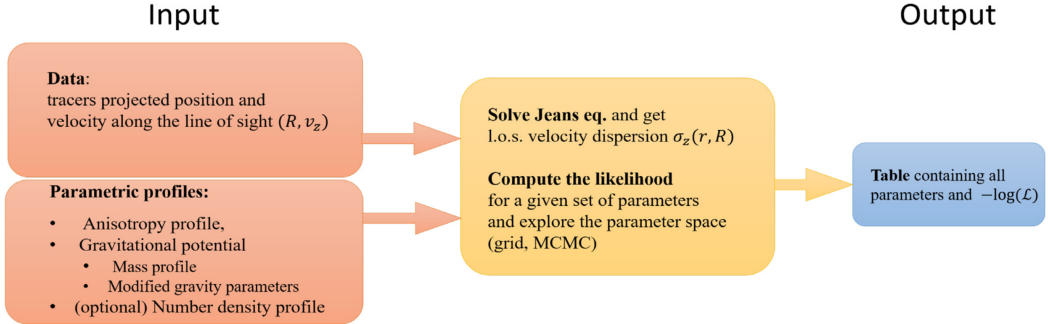


Figure 4.1: Flux diagram MG-MAMPOSSt. Figure 1 in ref. [63].

eter is distributed around a preferred central value with some standard deviation. The final results are a series of posteriors found and  $-\log(\mathcal{L})$ .

In figure 4.1, the steps performed by the code are outlined and summarized.

It's important to notice that the anisotropy profile is not known at the beginning. For this reason, many models are available<sup>2</sup>, but in this thesis, two models are adopted: generalized Tiret model, indicated gT (see e.g. ref. [42]), and Biviano&Pizzuti model (BP). Generalized Tiret profile has the following functional form:

$$\beta_{gT}(r) = \beta_0 + (\beta_\infty - \beta_0) \frac{r}{r + r_\beta}, \quad (4.1)$$

where  $\beta_0$  is the anisotropy in the center of the cluster and  $\beta_\infty$  is the anisotropy for  $r \rightarrow \infty$ , with transition radius fixed by  $r_\beta$  (ref. [61]). While the BP profile presents the following analytical distribution

$$\beta(r) = \beta_0 + (\beta_\infty - \beta_0) \frac{r}{r + r_\beta} + \beta_\infty \frac{r^2}{r_\beta^2} \exp\left[-\left(\frac{r}{r_\beta}\right)^2\right]. \quad (4.2)$$

As for the number density profile of the galaxies, we will always assume a NFW model. This choice is not causal, but based on ref. [4], where the spectroscopic data were corrected to compensate for the incompleteness at different clustercentric radii due to the different depths with which VIMOS and MUSE observed galaxies. After the correction, projected NFW proves suitable for fitting the number density of galaxies. This is clearly visible in the following plot.

The analytical expression for the dispersion of radial velocities can be found by integrating the Jeans equation (3.35) and can be written as follows (ref. [63], [43])

$$\sigma_r^2(r) = \frac{1}{\nu(r)} \int_r^\infty \exp\left(2 \int_r^s \frac{\beta(t)}{t} dt\right) \nu(s) \frac{d\Phi}{ds} ds, \quad (4.3)$$

<sup>2</sup>See ref. [61] to explore all models in MG-MAMPOSSt.

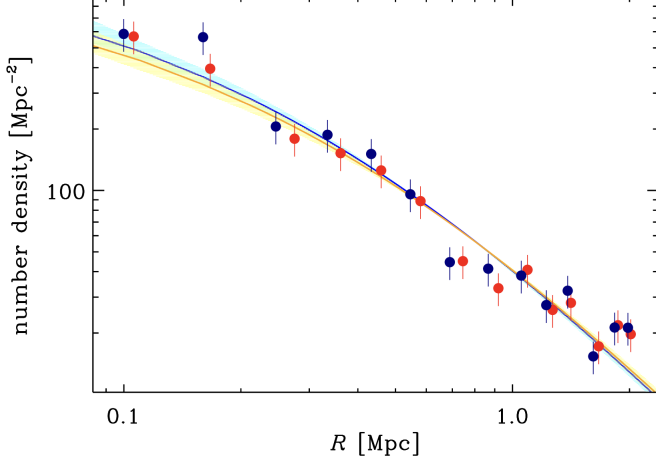


Figure 4.2: Plot show projected number density profiles of cluster members. In particular, we are only interested in the CLUMPS selected members, marked with red dots. The orange line represents the best fit and the yellow area a confidence interval equal to  $1\sigma$ . Figure 5 in ref. [4].

where the local velocity dispersion along the line of sight is

$$\sigma_z^2(r, R) = \left[ 1 - \beta(r) \left( \frac{R}{r} \right)^2 \right]. \quad (4.4)$$

Finally, the code output is the probability to observe a galaxy with position  $R_i$  and velocity dispersion  $v_{z,i}$  with  $\theta$  that represents a set of parameters. In these terms, the output is the following:

$$-\ln \mathcal{L} = - \sum_{i=1}^N \ln q(R_i, v_{z,i} | \theta), \quad (4.5)$$

where  $\mathcal{L}$  is the likelihood,  $N$  is the number of galaxies in the projected phase space,  $\theta$  is a set of parameters and  $q(R_i, v_{z,i})$  is the probability of observing a galaxy with projected position  $R_i$  and l.o.s  $v_{z,i}$ . This probability is analytically written as

$$q(R, v_z) = \frac{2\pi R g(R, v_z)}{N_{\text{proj}}(R_{\max}) - N_{\text{proj}}(R_{\min})}, \quad (4.6)$$

where  $N_{\text{proj}}(R)$  is the number of galaxies in the projected cylinder. Instead  $g(R, v_z)$  is the surface density of the observed objects

$$g(R, v_z) = \sqrt{\frac{2}{\pi}} \int_R^\infty \frac{r \nu(r)}{\sigma_z(R, r) \sqrt{r^2 - R^2}} \exp\left(-\frac{v_z^2}{2\sigma_z^2(R, r)}\right) dr. \quad (4.7)$$

The version of the code we are using is equipped with a module to fit the velocity distribution of the BCG; this modifies the likelihood in the following form

$$\mathcal{L}_{\text{kyn}}(\theta) = \mathcal{L}_{\text{MAMPOSST}}(\theta) + \frac{\chi^2_{BCG}(\theta)}{2}, \quad (4.8)$$

where  $\chi^2$  is the chi-square obtained between the theoretical prediction of  $\sigma_{teo}^2$  and the observed data points  $\sigma_{obs}^2$  of the BCG.

## 4.1 Kinematic analysis of MACS 1206

As we said in the previous chapter, we will study the cluster called MACS 1206 due to its physical properties; it performs well under the assumptions of spherical symmetry and dynamical relaxation. The reconstruction of the mass profile occurs via a multi-component approach, in fact each component is modeled differently and the sum of the component provides the total mass of the cluster

$$M_{\text{tot}}(r) = M_{\text{DM}}(r) + M_{\text{ICM}}(r) + M_{\text{BCG}}(r) + M_*(r), \quad (4.9)$$

where  $M_{\text{DM}}$  stand for dark matter mass profile and it is modeled with a gNFW profile described in Chapter 2, the reason why we chose the gNFW and not the NFW is  $\gamma$  dependence that provides information about the nature of dark matter.  $M_{\text{BCG}}$  is the mass profile of the Brightest Cluster Galaxy which we modeled with a Jaffe profile (3.4) and Jaffe's radius fixed at  $r_J = 0.039$  Mpc.

For the ICM profile, we have adopted two different ways: in the first one we used a beta profile with a beta exponent equal to 1 and, in the second one we have previously fitted the gas data with a beta profile, obtaining the parameters that characterize the latter. In the end, for the other galaxies (excluding BCG) we adopted a pNFW profile. The result of this fit can be found in table 4.1.

Parameter	Value	Error (within $1\sigma$ )	Unit
$\rho_0$	$4.51 \cdot 10^{14}$	$4.12 \cdot 10^{12}$	$M_\odot \text{ Mpc}^{-3}$
$r_c$	0.17	$0.17 \cdot 10^{-2}$	Mpc
$\alpha$	0.67	$0.23 \cdot 10^{-2}$	-

Table 4.1: Fit for  $\beta$  profile, note that  $\beta$  is almost 2/3.

Before the analysis, we have to set some cosmological parameters; in particular, the following fixed values are used:  $H_0 = 70 \text{ km s}^{-1} \text{ Mpc}^{-1}$  at  $z = 0$ , the redshift of the cluster  $z = 0.4398$ , the matter density  $\Omega_m = 0.3$  and dark energy density  $\Omega_\Lambda = 0.7$ .

These parameters remain constant and the same for each run of the code. In order to eliminate any interlopes in our sample, a specific method is developed according to ref. [4]. CLUster Membership in Phase Space (or CLUMPS) is based on the determination of peaks in the velocity distribution of galaxies in function of the clustercentric distance (distance from the center of the cluster). In the end, velocity boundaries are defined thanks to the minimum around the velocity peak and interlopers are removed (see ref. [3] for more details). Other methods are also developed such as P+G and CLEAN but they are not used in this thesis. The sample includes 468 galaxies (tracers), and 463 were used by the code to fit in a radial range between 0.055 Mpc and 2.153 Mpc in MCMC mode with an MCMC sample 110 000 points in the parameter space.

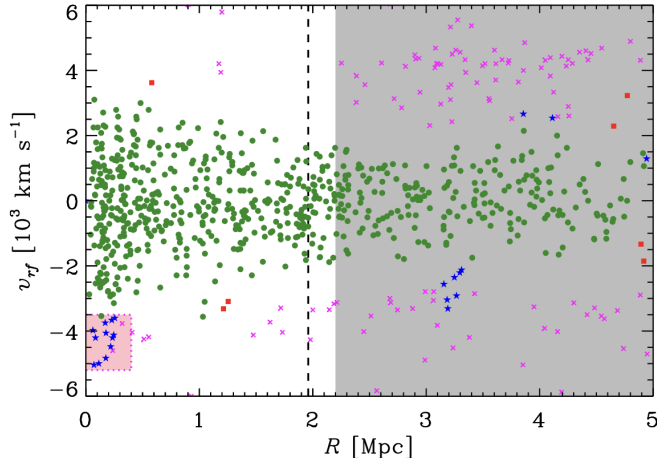


Figure 4.3: Projected space phase for MACS 1206, the pink enta area indicates galaxies that are not selected as members. The vertical dashed line indicates the virial radius. The gray area has not been considered as it is located at radii greater than 2.2 Mpc. The red squared are members selected by CLUMPS, blue stars are selected by P+G, green dots indicate members selected by CLUMPS and P+G. In Finally, magenta stars indicate members not selected by these two methods. Figure 1 in ref. [4].

Furthermore, it is important to say that different velocity anisotropy models were used for BCG and for the rest of the cluster; in fact, for BCG we choose an Osipkov-Merritt, or more simply "OM" (ref. [57], [46]) and follow this analytical

distribution

$$\beta_{BCG}(r) = \frac{r^2}{r^2 + r_a^2}, \quad (4.10)$$

where  $r_a$  is the scale radius set to 20 Mpc. With this value, the OM profile is almost constant in the entire range.

Instead, for the anisotropy model of the rest of the cluster, we adopted two different profiles in order to find the best. The gT anisotropy profile (4.1) and BP profile (4.2) which we introduced previously.

In MG-MAMPOSSt, the velocity anisotropy of member galaxies is actually defined in terms of the rescaled parameters  $\mathcal{A}_0$  and  $\mathcal{A}_\infty$  through the relation  $\mathcal{A}_0 = (\sigma_r/\sigma_\theta)_0 = (1 - \beta_0)^{-1/2}$  and similarly  $\mathcal{A}_\infty = (\sigma_r/\sigma_\theta)_\infty = (1 - \beta_\infty)^{-1/2}$ .

Overall, the analysis consists of 4 MG-MAMPOSSt runs: in the first, a gT type model is used for the anisotropy, leaving the  $r_\beta$  parameter free; in the second run, the same procedure is performed with a BP type model for the anisotropy; a third run employs a BP model for the anisotropy with  $r_\beta$  fixed; in particular we decided to set  $r_\beta = 1$  Mpc because Mpc is the typical dimension for a cluster galaxy. Instead, the last run was performed with a BP anisotropy model but a different beta profile because the exponent  $\beta$  in profile (3.1) was set equal to 2/3 instead of equal to one as in the first three mentioned above.

So we have a total of 8 free parameters listed in the following table, together with the lower and upper limits imposed through flat priors.

Parameter	Lower limit	Upper limit	Unit
$r_{200}$	0.50	5.00	Mpc
$r_\nu$ (tracer scale)	0.39	0.54	Mpc
$r_s$	0.04	3.90	Mpc
$\mathcal{A}_\infty$ (anisotropy, outer)	0.30	5.10	-
$\mathcal{A}_0$ (anisotropy, central)	0.50	4.10	-
$X_L$	2.01	7.00	$M_\odot/L_\odot$
$\gamma$ (gNFW inner slope)	0.30	2.00	-
$r_\beta$	0.03	3.10	Mpc

Table 4.2: The 8 free parameters with their lower and upper limits and their units.

## 4.2 Results

The results of the four scenarios discussed above are listed in table 4.3, where we list the constraints on the parameters at  $2\sigma$ .

$\beta$ model	$r_{200}$ [Mpc]	$r_\nu$ [Mpc]	$r_s$ [Mpc]	$\mathcal{A}_\infty$	$\gamma$	$\mathcal{A}_0$	$r_\beta$ [Mpc]	$X_L$ [ $M_\odot/L_\odot$ ]
gT ( $r_\beta$ free)	$2.02^{+0.20}_{-0.18}$	$0.41^{+0.04}_{-0.02}$	$0.53^{+0.32}_{-0.22}$	$2.75^{+1.96}_{-1.39}$	$0.57^{+0.28}_{-0.26}$	$1.28^{+1.16}_{-0.87}$	$0.42^{+1.46}_{-0.45}$	$4.46^{+0.21}_{-0.23}$
BP ( $r_\beta$ free)	$2.03^{+0.20}_{-0.19}$	$0.41^{+0.03}_{-0.02}$	$0.54^{+0.36}_{-0.24}$	$2.70^{+2.00}_{-1.53}$	$0.57^{+0.29}_{-0.26}$	$1.07^{+1.06}_{-0.62}$	$0.37^{+2.25}_{-0.48}$	$4.46^{+0.22}_{-0.23}$
BP ( $r_\beta$ fixed)	$2.02^{+0.23}_{-0.21}$	$0.41^{+0.03}_{-0.02}$	$0.51^{+0.70}_{-0.23}$	$2.62^{+2.12}_{-1.47}$	$0.51^{+0.37}_{-0.22}$	$1.20^{+0.73}_{-0.42}$	—	$4.48^{+0.22}_{-0.25}$
BP ( $r_\beta$ free)*	$1.96^{+0.33}_{-0.36}$	$0.41^{+0.04}_{-0.02}$	$0.46^{+0.35}_{-0.27}$	$2.85^{+1.90}_{-1.57}$	$0.47^{+0.39}_{-0.40}$	$1.01^{+0.89}_{-0.59}$	$0.40^{+2.32}_{-0.40}$	$4.50^{+0.26}_{-0.27}$

Table 4.3: Results of the four runs performed with BP and gT anisotropy models. For each parameter the median and the 95% credible interval are reported. In the case of BP with fixed  $r_\beta$ , the transition radius is not a free parameter.

\* This run also includes the fit of the gas component.

From the results in table 4.3, it is possible to notice that, with the same number of free parameters, the gT model and the BP model give substantially identical results for  $\gamma$ .

To qualitatively determine which was better among the runs with the BP pattern (one with and the other without free  $r_\beta$ ), we use the Bayesian Information Criterion (BIC hereafter) defined as follows

$$\text{BIC} = k \ln n - 2 \ln \mathcal{L}, \quad (4.11)$$

where  $k$  is the number of parameters,  $n$  the size of sample and  $\mathcal{L}$  the likelihood value. In this case all samples were composed, as said before, from 463 explored galaxies. The code returns the  $-\ln \mathcal{L}$  and it is therefore easy to check that the BP model with  $r_\beta$  free is favored thanks to a  $\text{BIC} = 8628.14$  against a  $\text{BIC} = 8633.84$  for the fixed  $r_\beta$ . You consequently have a  $\Delta\text{BIC} = 5.70$ .

We therefore decided to focus on the BP model with free  $r_\beta$  which, from the BIC value, proved to be the most promising model.

$r_{200}$  represents the virial radius of dark matter halo, defined as the distance from the center within which the average density of the dark matter halo is 200 times the critical density of the universe. For MACS 1206, this radius is about 2 Mpc in every analysis. Physically,  $r_{200}$  bounds the gravitationally bound region of the cluster and provides a scale of magnitude: outside this radius, the density drops below 200 times the critical density, and the material is no longer tightly bound to the cluster.

$r_\nu$  is the scale radius of the radial distribution of galaxies that are members of the cluster. In this case  $r_\nu$  is smaller than  $r_{200}$ , so that means that galaxies are distributed in a more concentrated way than dark matter and, in particular, closer

to the center of the cluster.

$r_s$  is the scale radius of the gNFW profile and represents the scale beyond which the density profile begins to decline most rapidly.

As it concerns  $r_\beta$ , the transition radius of the anisotropy, it is possible to notice how the latter is very close to zero, this indicates an almost constant anisotropy from the center of the cluster to the outermost regions. More generally, this was found to be true for both the gT model and the BP model.

Focusing instead on the  $\gamma$  parameter of the gNFW, our main object of interest, we obtain e.g.  $\gamma = 0.57^{+0.29}_{-0.26}$  for the BP- $r_\beta$ -free model, lower than the value found in ref. [4]. This is valid in all the tested scenarios.

We recall here that  $\gamma$  describes the internal slope of the dark matter density profile in the cluster. In case of a pure NFW we have  $\gamma = 1$  but a smaller value indicates a density towards the center that grows flatter, creating a less cuspidate profile and more cores.

When further changing the fit to the gas mass data in the fourth run of Table 4.2 (where we used  $\beta = 2/3$  in (3.1)<sup>3</sup>, providing a better fit with respect to the case  $\beta = 1$ ) we obtain an even lower value. This is extremely important because, as we discussed before,  $\gamma$  may be indicative about the type and interaction of dark matter, bringing also information of any possible baryonic feedback. Coming back to  $\gamma$ , this is lower but still within the limits of a slope generated by cold dark matter within the standard cosmological model.

Also, from the figure 4.4 it is possible to see how  $X_L$  tends to follow a trend opposite to  $\gamma$ , as the mass/brightness ratio increases the  $\gamma$  parameter decreases and vice versa. This remains valid in all regimes used, both gT and BP. Consequently, this seems to indicate that a greater presence of baryonic mass tends to make the dark matter slope less steep.

---

<sup>3</sup>Note that here, the  $\beta$  parameter is the exponent used in the radial distribution for gas.

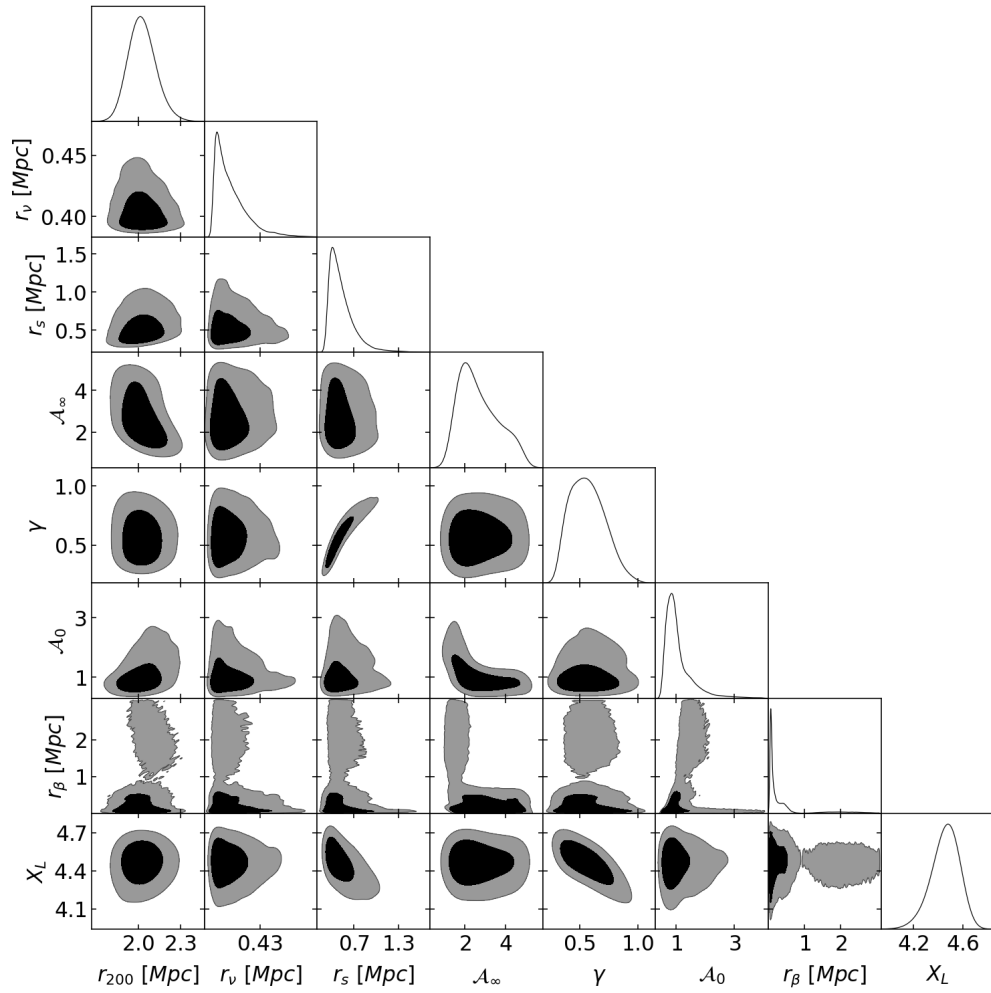


Figure 4.4: Marginal distributions of parameters in the BP model with free  $r_\beta$ . The darker region indicates the uncertainty interval equal to  $1\sigma$  (68 %) and the gray zone an uncertainty interval equal to  $2\sigma$  (95 %).

### Decomposition of mass

In fig. 4.5 the total kinematic mass distribution obtained with MG-MAMPOSST is reported. The plot shows how, at very small radii, the BCG contribution dominates, only to be overtaken by dark matter while BCG mass becomes constant. This is expected because BCG has a radius measured in kpc. It's also important to note that although the contribution of galaxies, and especially gas, increases considerably, dark matter remains predominant all the way to the outermost regions, almost matching the cluster's overall mass profile. This behavior is completely analogous in every run conducted, thus underlining the importance of dark matter and how this is actually the main component of the cluster.

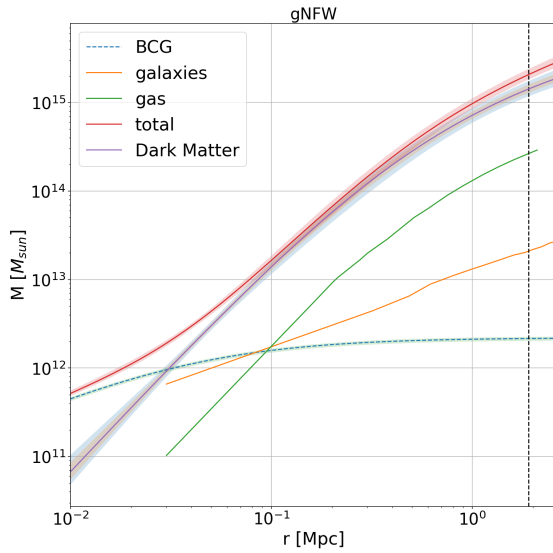


Figure 4.5: Mass decomposition with BP model and free  $r_\beta$ . The dashed vertical line represents the upper limit of the radial range used for the fit, with a value equal to 2.153 Mpc.

### Anisotropy profile

In fig. 4.6 we can see the anisotropy profile for the first three runs described above. The reconstruction of  $\beta(r)$  shows moderately radial orbits already at the center and a growth towards more radial values as the radius increases. The black curve in fact starts around  $\beta \sim 0.4$  and tends asymptotically to  $\beta \sim 0.75$  beyond 1 Mpc. Here too, the confidence bands are indicated with a darker color within  $1\sigma$  and lighter within  $2\sigma$ .

$A_0$  is related to central anisotropy, that is, how the velocities of galaxies near the center of the cluster are oriented. From the plot you can see how in the gT model

the anisotropy for  $r \rightarrow 0$  is  $\sim 0.4$ , compatible with a weak radial anisotropy. This means that, near nucleus, galaxies move with very similar speeds in all directions.  $\mathcal{A}_\infty$  is related to anisotropy at large distances and  $\beta$  grows indicating markedly radial orbits towards the peripheries of the cluster.

In the BP model, with and without  $r_\beta$  fixed,  $\beta$  start from  $\sim 0.25$ , which indicate more isotropic orbits where the radial and tangential directions are equivalent.

It's interesting to note the bump in the anisotropy profile in the BP template with  $r_\beta$  fixed (center plot). This result does not have a strictly physical nature; it is due to the rigidity on the position of the transition from  $\beta_0$  to  $\beta_\infty$ . In fact, forcing the transition to a fixed radius, fit introduce a local curvature to better adapt velocity dispersions. This is demonstrated precisely by the plot of the BP model but having a free  $r_\beta$  (right plot), in this case the bump is significantly reduced. Finally, the gT model instead adopts a softer profile which, thanks to a free beam, completely eliminates this bump (left plot).

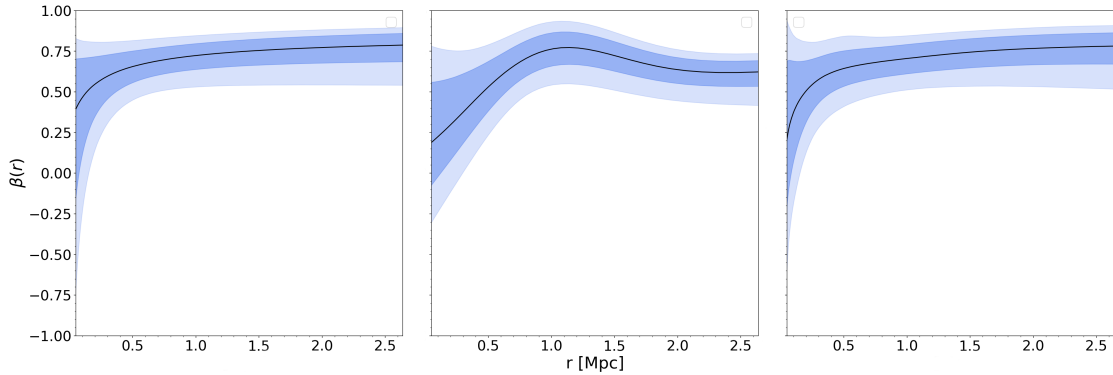


Figure 4.6: **Left panel:** anisotropy profile for gT model and free  $r_\beta$ . **Center panel:** BP model with fixed  $r_\beta$ , showing a clear bump in the anisotropy profile. **Right panel:** BP model with free  $r_\beta$ , with a smaller bump around  $r \sim 0.5$  Mpc. In each panel, the darker region corresponds to  $1\sigma$  uncertainty, and the lighter to  $2\sigma$ .



# Chapter 5

## Conclusions

In this thesis we have derived the total multi-component mass profile of the galaxy cluster MACS J1206.2-0847 by employing a kinematic reconstruction with the MG-MAMPOSST procedure. We accounted for both the distribution of the member galaxies in the projected phase space and the velocity dispersion of the BCG to perform a detailed reconstruction of the mass down to 1 kpc from the cluster center, identified with the center of the BCG. Assuming a gNFW for the dark matter density profile, we have estimated a gNFW a slope  $\gamma = 0.57^{+0.29}_{-0.27}$ , a value slightly lower than expected from the  $\Lambda$ CDM model where  $\gamma = 1$  and also lower than the values found in ref. [4] that we use for comparison. The difference corresponds to a weak tension ( $\lesssim 2\sigma$ ), in fact, considering the uncertainties, this "intermediate" value  $\gamma$  is consistent with an inclusive model of interactions with baryonic matter (ref. [54], [20]). In other words, the cluster shows a more core and less cuspidate profile at the center, this suggests the presence of baryon process such as interaction with hot gas, star formation and supernovae phenomena that have modified the distribution of the dark matter in the cluster. Furthermore, the differences shown with respect ref. [4] are also due to the correction of numerical problem in the implementation of the gas and galaxy profile.

These results underline the need and importance of detailed kinematic analysis conducted on galaxy clusters to increasingly test the predictions of the cosmological standard model with greater precision. In particular, the importance of using the contributions given by BCG and gas is underlined. Furthermore, as seen in Chapter 4, different anisotropy models do not lead to significantly different results, making an accurate choice not so necessary to obtain plausible results.

Despite the results obtained, it is also important to recognize some limitations present in the analysis conducted. First of all, the need to use clusters having spherical symmetry and under the hypothesis of dynamic relaxation. This represents a challenge for future studies given that many clusters do not lend themselves well to respecting these hypotheses (for example, clusters in merging phase or with

a large number of substructures). In such cases, departure of the assumptions of the Jeans' analysis may lead to bias in the reconstructed dark matter profile. In order to mitigate effects due to the internal physics of a single cluster, would be necessary to extend the analysis performed here to larger sample of objects and derive robust constraints on  $\gamma$  that may add crucial information of the nature of the dark matter in the universe. Moreover, the inclusion of the information provided by independent probes of the mass in clusters may help in breaking the degeneracy in the model parameters and in better quantifying the impact of systematics. For this reason, the next step of this work will be a combination of the kinematic analysis with the data from strong and weak gravitational lensing obtained within the CLASH project (see e.g. ref. [80]).

From this perspective, future surveys will play a crucial role and the combination of spectroscopic analysis obtained from ground-based telescopes, with data coming from telescopes such as Euclid capable of studying lensing phenomena in extreme detail (ref. [45]), will allow us to answer questions that are still unanswered.

# Bibliography

1. Aghanim, N. *et al.* Planck2018 results: VI. Cosmological parameters. *Astronomy & Astrophysics* **641**, A6. ISSN: 1432-0746. <http://dx.doi.org/10.1051/0004-6361/201833910> (Sept. 2020).
2. Annunziatella, M. *et al.* CLASH-VLT: The stellar mass function and stellar mass density profile of the  $z=0.44$  cluster of galaxies MACS J1206.2-0847. *Astronomy and Astrophysics* **571**, A80. ISSN: 1432-0746. <http://dx.doi.org/10.1051/0004-6361/201424102> (Nov. 2014).
3. Biviano, A. *et al.* The GOGREEN survey: Internal dynamics of clusters of galaxies at redshift 0.9–1.4. *Astronomy and Astrophysics* **650**, A105. ISSN: 1432-0746. <http://dx.doi.org/10.1051/0004-6361/202140564> (June 2021).
4. Biviano, A. *et al.* CLASH-VLT: The Inner Slope of the MACS J1206.2-0847 Dark Matter Density Profile. *The Astrophysical Journal* **958**, 148 (Nov. 2023).
5. Brooks, A. M., Kuhlen, M., Zolotov, A. & Hooper, D. A BARYONIC SOLUTION TO THE MISSING SATELLITES PROBLEM. *The Astrophysical Journal* **765**, 22. ISSN: 1538-4357. <http://dx.doi.org/10.1088/0004-637X/765/1/22> (Feb. 2013).
6. Burkert, A. The Structure of Dark Matter Halos in Dwarf Galaxies. **447**, L25–L28. arXiv: [astro-ph/9504041 \[astro-ph\]](https://arxiv.org/abs/astro-ph/9504041) (July 1995).
7. Cameron, E., Driver, S. P., Graham, A. W. & Liske, J. THE MILLENNIUM GALAXY CATALOGUE: EXPLORING THE COLOR-CONCENTRATION BIMODALITY VIA BULGE-DISK DECOMPOSITION. *The Astrophysical Journal* **699**, 105–117. ISSN: 1538-4357. <http://dx.doi.org/10.1088/0004-637X/699/1/105> (June 2009).
8. Caminha, G. B. *et al.* Mass distribution in the core of MACS J1206: Robust modeling from an exceptionally large sample of central multiple images. *Astronomy and Astrophysics* **607**, A93. ISSN: 1432-0746. <http://dx.doi.org/10.1051/0004-6361/201731498> (Nov. 2017).

9. Capozziello, S., Cardone, V. F. & Troisi, A. Dark energy and dark matter as curvature effects? *Journal of Cosmology and Astroparticle Physics* **2006**, 001–001. ISSN: 1475-7516. <http://dx.doi.org/10.1088/1475-7516/2006/08/001> (Aug. 2006).
10. Cavaliere, A. G., Gursky, H. & Tucker, W. H. Extragalactic X-ray Sources and Associations of Galaxies. *Nature* **231**, 437–438. ISSN: 1476-4687 (June 1971).
11. Chandra X-ray Observatory. *Pandora's Cluster (Abell 2744)* Accessed on 17 June 2025. <https://chandra.harvard.edu/photo/2011/a2744/>.
12. Choudhury, T. R. *Lecture 11 - Relativistic perturbation theory in cosmology* <http://www.ncra.tifr.res.in:8081/~tirth/Teaching/Cosmology-2021/Lectures/lecture-11-web.pdf>. Accessed: 2025-06-28. 2021.
13. CLASH-VLT Collaboration. *CLASH-VLT Public Web Page* <https://sites.google.com/site/vltclashpublic/home>. Accessed: 2025-07-16.
14. Clowe, D. *et al.* A Direct Empirical Proof of the Existence of Dark Matter. *The Astrophysical Journal* **648**, L109–L113. ISSN: 1538-4357. <http://dx.doi.org/10.1086/508162> (Aug. 2006).
15. Cowie, L. L. & Binney, J. Radiative regulation of gas flow within clusters of galaxies: a model for cluster X-ray sources. **215**, 723–732 (Aug. 1977).
16. David J. E. Marsh, D. E. & Mehta, V. M. *Dark Matter: Evidence, Theory and Constraints* ISBN: 978-0-691-24951-3 (Princeton UniversityPress, 2024).
17. De Bernardis, P. *et al.* A flat Universe from high-resolution maps of the cosmic microwave background radiation. *Nature* **404**, 955–959. ISSN: 1476-4687. <http://dx.doi.org/10.1038/35010035> (Apr. 2000).
18. De Propris, R. *et al.* Brightest cluster galaxies: the centre can(not?) hold. *Monthly Notices of the Royal Astronomical Society* **500**, 310–318. ISSN: 1365-2966. <http://dx.doi.org/10.1093/mnras/staa3286> (Oct. 2020).
19. de Vaucouleurs, G. Recherches sur les Nebuleuses Extragalactiques. *Annales d'Astrophysique* **11**, 247 (Jan. 1948).
20. Del Popolo, A. & Le Delliou, M. Review of Solutions to the Cusp-Core Problem of the CDM Model. *Galaxies* **9**. ISSN: 2075-4434. <https://www.mdpi.com/2075-4434/9/4/123> (2021).
21. DESI Collaboration *et al.* DESI DR2 Results II: Measurements of Baryon Acoustic Oscillations and Cosmological Constraints. *arXiv e-prints*, arXiv:2503.14738. arXiv: 2503.14738 [astro-ph.CO] (Mar. 2025).

22. Dyson, F. W., Eddington, A. S. & Davidson, C. IX. A determination of the deflection of light by the sun's gravitational field, from observations made at the total eclipse of May 29, 1919. *Philosophical Transactions of the Royal Society of London. Series A, Containing Papers of a Mathematical or Physical Character* **220**, 291–333. eprint: <https://royalsocietypublishing.org/doi/pdf/10.1098/rsta.1920.0009>. <https://royalsocietypublishing.org/doi/abs/10.1098/rsta.1920.0009> (1920).
23. Ebeling, H. *et al.* A Spectacular Giant Arc in the Massive Cluster Lens MACS J1206.2–0847. *Monthly Notices of the Royal Astronomical Society* **395**, 1213–1224 (2009).
24. Eckert, D. *et al.* Constraints on dark matter self-interaction from the internal density profiles of X-COP galaxy clusters. *AA* **666**, A41. <https://doi.org/10.1051/0004-6361/202243205> (2022).
25. Erfanianfar, G. *et al.* Stellar mass–halo mass relation for the brightest central galaxies of X-ray clusters since z0.65. *AA* **631**, A175. <https://doi.org/10.1051/0004-6361/201935375> (2019).
26. ESA - Planck Satellite Mission. *Immagine del satellite Planck in orbita* <http://www.satelliteplanck.it/content/view/92/55/index.html>. Accesso il 14 luglio 2025. 2009.
27. ESA/Hubble NASA. *A Perfect Spiral - Hubble Image of Galaxy NGC 4911* Accessed: July 3, 2025. 2011. <https://esahubble.org/images/heic1115a/>.
28. Ettori, S. *et al.* Mass profiles and cMDM relation in X-ray luminous galaxy clusters (Corrigendum). *Astronomy and Astrophysics* **526**, C1. ISSN: 1432-0746. <http://dx.doi.org/10.1051/0004-6361/201015271e> (Jan. 2011).
29. Ezquiaga, J. M. & Zumalacarregui, M. Dark Energy in Light of Multi-Messenger Gravitational-Wave Astronomy. *Frontiers in Astronomy and Space Sciences* **5** (Dec. 2018).
30. Fabricant, D., Lecar, M. & Gorenstein, P. X-ray measurements of the mass of M 87. **241**, 552–560 (Oct. 1980).
31. Forman, W., Kellogg, E., Gursky, H., Tananbaum, H. & Giacconi, R. Observations of the Extended X-Ray Sources in the Perseus and Coma Clusters from UHURU. **178**, 309–316 (Dec. 1972).
32. Friedmann, A. Über die Krümmung des Raumes. *Zeitschrift für Physik* **10**, 377–386 (Jan. 1922).
33. Geek3. *Universe scale evolution plot* [https://commons.wikimedia.org/wiki/File:Mplwp\\_universe\\_scale\\_evolution.svg](https://commons.wikimedia.org/wiki/File:Mplwp_universe_scale_evolution.svg). Licensed under Creative Commons Attribution-ShareAlike 3.0. 2011.

34. Girardi, M. *et al.* CLASH-VLT: Substructure in the galaxy cluster MACS J1206.2-0847 from kinematics of galaxy populations. **579**, A4. arXiv: 1503.05607 [astro-ph.CO] (July 2015).
35. Gonzalez, A. H., Zaritsky, D. & Zabludoff, A. I. A Census of Baryons in Galaxy Clusters and Groups. *The Astrophysical Journal* **666**, 147–155. ISSN: 1538-4357. <http://dx.doi.org/10.1086/519729> (Sept. 2007).
36. Jaffe, W. A simple model for the distribution of light in spherical galaxies. **202**, 995–999 (Mar. 1983).
37. Kim, S. Y., Peter, A. H. G. & Hargis, J. R. Missing Satellites Problem: Completeness Corrections to the Number of Satellite Galaxies in the Milky Way are Consistent with Cold Dark Matter Predictions. *Physical Review Letters* **121**. ISSN: 1079-7114. <http://dx.doi.org/10.1103/PhysRevLett.121.211302> (Nov. 2018).
38. King, I. The structure of star clusters. I. an empirical density law. **67**, 471 (Oct. 1962).
39. Koposov, S. *et al.* The Luminosity Function of the Milky Way Satellites. *The Astrophysical Journal* **686**, 279–291. ISSN: 1538-4357. <http://dx.doi.org/10.1086/589911> (Oct. 2008).
40. Langlois, D. *Degenerate Higher-Order Scalar-Tensor (DHOST) theories* 2018. arXiv: 1707.03625 [gr-qc]. <https://arxiv.org/abs/1707.03625>.
41. Longair, M. S. *Galaxy Formation* ISBN: 978-3-662-65890-1 (Springer Berlin, Heidelberg, 2023).
42. Mamon, G. A. *et al.* Structural and dynamical modeling of WINGS clusters: II. The orbital anisotropies of elliptical, spiral, and lenticular galaxies. *Astronomy amp; Astrophysics* **631**, A131. ISSN: 1432-0746. <http://dx.doi.org/10.1051/0004-6361/201935081> (Nov. 2019).
43. Mamon, G. A., Biviano, A. & Boué, G. MAMPOSSt: Modelling Anisotropy and Mass Profiles of Observed Spherical Systems – I. Gaussian 3D velocities. *Monthly Notices of the Royal Astronomical Society* **429**, 3079–3098. ISSN: 0035-8711. eprint: <https://academic.oup.com/mnras/article-pdf/429/4/3079/3298617/sts565.pdf>. <https://doi.org/10.1093/mnras/sts565> (Jan. 2013).
44. Maoz, D. *Astrophysics in a Nutshell. Second Edition* (2016).
45. Mellier, Y. *et al.* Euclid: I. Overview of the Euclid mission. *Astronomy amp; Astrophysics* **697**, A1. ISSN: 1432-0746. <http://dx.doi.org/10.1051/0004-6361/202450810> (Apr. 2025).

46. Merritt, D. Distribution functions for spherical galaxies. **214**, 25P–28P (June 1985).
47. Milgrom, M. A modification of the Newtonian dynamics as a possible alternative to the hidden mass hypothesis. **270**, 365–370 (July 1983).
48. Mo, H., van den Bosch, F. C. & White, S. *Galaxy Formation and Evolution* (2010).
49. Müller, Oliver *et al.* A too-many-dwarf-galaxy-satellites problem in the M 83 group. *AA* **684**, L6. <https://doi.org/10.1051/0004-6361/202348969> (2024).
50. Narayan, R. & Bartelmann, M. *Lectures on Gravitational Lensing* 1997. arXiv: astro-ph/9606001 [astro-ph]. <https://arxiv.org/abs/astro-ph/9606001>.
51. NASA/GSFC. *Servicing Mission 4 (SM4): COS and WFC3 Installation on HST* <https://science.nasa.gov/mission/hubble/observatory/missions-to-hubble/servicing-mission-4/>. accessed 16 July 2025. 2009.
52. Navarro, J. F., Frenk, C. S. & White, S. D. M. The Structure of Cold Dark Matter Halos. *The Astrophysical Journal* **462**, 563. ISSN: 1538-4357. <http://dx.doi.org/10.1086/177173> (May 1996).
53. Navarro, J. F., Frenk, C. S. & White, S. D. M. A Universal Density Profile from Hierarchical Clustering. *The Astrophysical Journal* **490**, 493–508. ISSN: 1538-4357. <http://dx.doi.org/10.1086/304888> (Dec. 1997).
54. Newman, A. B., Treu, T., Ellis, R. S. & Sand, D. J. THE DENSITY PROFILES OF MASSIVE, RELAXED GALAXY CLUSTERS. II. SEPARATING LUMINOUS AND DARK MATTER IN CLUSTER CORES. *The Astrophysical Journal* **765**, 25. ISSN: 1538-4357. <http://dx.doi.org/10.1088/0004-637X/765/1/25> (Feb. 2013).
55. Neyrinck, M. C. Quantifying distortions of the Lagrangian dark-matter mesh in cosmology. *Monthly Notices of the Royal Astronomical Society* **428**, 141–153. ISSN: 0035-8711. <http://dx.doi.org/10.1093/mnras/sts027> (Oct. 2012).
56. O’Riordan, C. M. *et al.* Euclid: A complete Einstein ring in NGC 6505. *AA* **694**, A145. <https://doi.org/10.1051/0004-6361/202453014> (2025).
57. Osipkov, L. P. Spherical systems of gravitating bodies with an ellipsoidal velocity distribution. *Soviet Astronomy Letters* **5**, 42–44 (Jan. 1979).
58. Ostriker, J. P. & Hausman, M. A. Cannibalism among the galaxies: dynamically produced evolution of cluster luminosity functions. **217**, L125–L129 (Nov. 1977).

59. Pascale, M. *et al.* *SN H0pe: The First Measurement of  $H_0$  from a Multiply-Imaged Type Ia Supernova, Discovered by JWST* 2024. arXiv: 2403.18902 [astro-ph.CO]. <https://arxiv.org/abs/2403.18902>.
60. Pizzuti, L., Fantoccoli, F., Broccolato, V., Biviano, A. & Diaferio, A. Testing refracted gravity with the kinematics of galaxy clusters. *Astronomy and Astrophysics* **698**, A83. ISSN: 1432-0746. <http://dx.doi.org/10.1051/0004-6361/202452739> (June 2025).
61. Pizzuti, L., Saltas, I. D., Biviano, A., Mamon, G. & Amendola, L. *MG-MAMPOSSt, a code to test gravity at galaxy-cluster scales: a technical introduction* 2022. arXiv: 2201.07194 [astro-ph.CO]. <https://arxiv.org/abs/2201.07194>.
62. Pizzuti, L. *Nature Of Gravity From The Mass Profiles Of Galaxy Clusters* PhD thesis (Università degli Studi di Trieste, 2017/2018).
63. Pizzuti, L., Saltas, I. D. & Amendola, L. MG-MAMPOSSt: a code to test modifications of gravity with internal kinematics and lensing analyses of galaxy clusters. *Monthly Notices of the Royal Astronomical Society* **506**, 595–612. ISSN: 1365-2966. <http://dx.doi.org/10.1093/mnras/stab1727> (June 2021).
64. Postman, M. *et al.* THE CLUSTER LENSING AND SUPERNOVA SURVEY WITH HUBBLE: AN OVERVIEW. *The Astrophysical Journal Supplement Series* **199**, 25. ISSN: 1538-4365. <http://dx.doi.org/10.1088/0067-0049/199/2/25> (Mar. 2012).
65. Ragagnin, A. *et al.* Dianoga SIDM: Galaxy cluster self-interacting dark matter simulations. *Astronomy and Astrophysics* **687**, A270. ISSN: 1432-0746. <http://dx.doi.org/10.1051/0004-6361/202449872> (July 2024).
66. Riess, A. G. *et al.* Observational Evidence from Supernovae for an Accelerating Universe and a Cosmological Constant. *The Astronomical Journal* **116**, 1009–1038. ISSN: 0004-6256. <http://dx.doi.org/10.1086/300499> (Sept. 1998).
67. Rosati, P., Balestra, I., Grillo, C., Mercurio, A. & et al. CLASH-VLT: A VIMOS Large Programme to Map the Dark Matter Mass Distribution in Galaxy Clusters and Probe Distant Lensed Galaxies. *The Messenger* **158**, 48–53. <https://www.eso.org/sci/publications/messenger/archive/no.158-dec14/messenger-no158-48-53.pdf> (2014).
68. Röttgering, H. J. A. *Lecture 10: Galaxies* Lecture notes, PDF. 2011. [https://home.strw.leidenuniv.nl/~rottgering/Site/Galaxies\\_lectures\\_2011\\_files/Lecture-10.pdf](https://home.strw.leidenuniv.nl/~rottgering/Site/Galaxies_lectures_2011_files/Lecture-10.pdf).

69. Rubin, V. C. & Ford Jr., W. K. Rotation of the Andromeda Nebula from a Spectroscopic Survey of Emission Regions. **159**, 379 (Feb. 1970).
70. Sachs, M. *Gravitational-lensing-3d (diagram showing the effects of gravitational lensing in 3D)* Wikimedia Commons. Dual-licensed under CC BY-SA 3.0 and GFDL 1.2 or later. Accessed 21 Aug 2025. 2008. <https://commons.wikimedia.org/wiki/File:Gravitational-lensing-3d.png>.
71. Sarazin, C. L. *X-Ray Emission from Clusters of Galaxies – Contents* NASA/I-PAC Extragalactic Database Level 5, California Institute of Technology. Accessed: 2025-08-01. Mar. 2002. [https://ned.ipac.caltech.edu/level5/March02/Sarazin/Sarazin\\_contents.html](https://ned.ipac.caltech.edu/level5/March02/Sarazin/Sarazin_contents.html).
72. Sartoris, B. *et al.* CLASH-VLT: a full dynamical reconstruction of the mass profile of Abell S1063 from 1 kpc out to the virial radius. *AA* **637**, A34. <https://doi.org/10.1051/0004-6361/202037521> (2020).
73. Sérsic, J. L. Influence of the atmospheric and instrumental dispersion on the brightness distribution in a galaxy. *Boletin de la Asociacion Argentina de Astronomia La Plata Argentina* **6**, 41–43 (Feb. 1963).
74. Space Telescope Science Institute. *CLASH: Cluster Lensing And Supernova survey with Hubble* <https://www.stsci.edu/~postman/CLASH/>. Accessed: 2025-07-15.
75. Spergel, D. N. & Steinhardt, P. J. Observational Evidence for Self-Interacting Cold Dark Matter. *Phys. Rev. Lett.* **84**, 3760–3763. <https://link.aps.org/doi/10.1103/PhysRevLett.84.3760> (17 Apr. 2000).
76. Springel, V. *et al.* Simulations of the formation, evolution and clustering of galaxies and quasars. **435**, 629–636. arXiv: [astro-ph/0504097](https://arxiv.org/abs/astro-ph/0504097) [astro-ph] (June 2005).
77. Springel, V., White, S. D. M., Jenkins, A. & et al. *The Millennium Simulation Project* <https://wwwmpa.mpa-garching.mpg.de/galform/virgo/millennium/>. Accessed: 2025-06-27. 2005.
78. Sunyaev, R. A. & Zeldovich, I. B. Microwave background radiation as a probe of the contemporary structure and history of the universe. **18**, 537–560 (Jan. 1980).
79. Umetsu, K. *et al.* CLASH: MASS DISTRIBUTION IN AND AROUND MACS J1206.2-0847 FROM A FULL CLUSTER LENSING ANALYSIS. *The Astrophysical Journal* **755**, 56. ISSN: 1538-4357. <http://dx.doi.org/10.1088/0004-637X/755/1/56> (July 2012).

80. Umetsu, K. *et al.* CLASH: JOINT ANALYSIS OF STRONG-LENSING, WEAK-LENSING SHEAR, AND MAGNIFICATION DATA FOR 20 GALAXY CLUSTERS\*. *The Astrophysical Journal* **821**, 116. ISSN: 1538-4357. <http://dx.doi.org/10.3847/0004-637X/821/2/116> (Apr. 2016).
81. Walsh, S. M., Willman, B. & Jerjen, H. THE INVISIBLES: A DETECTION ALGORITHM TO TRACE THE FAIEST MILKY WAY SATELLITES. *The Astronomical Journal* **137**, 450–469. ISSN: 1538-3881. <http://dx.doi.org/10.1088/0004-6256/137/1/450> (Dec. 2008).
82. Wikipedia contributors. *Comparison of NFW and Einasto profiles — Wikipedia* [https://en.wikipedia.org/wiki/File:Comparison\\_of\\_NFW\\_and\\_Einasto\\_profiles.svg](https://en.wikipedia.org/wiki/File:Comparison_of_NFW_and_Einasto_profiles.svg). Accessed: July 11, 2025. 2024.
83. Wyithe, J. S. B., Turner, E. L. & Spergel, D. N. Gravitational Lens Statistics for Generalized NFW Profiles: Parameter Degeneracy and Implications for Self-Interacting Cold Dark Matter. **555**, 504–523. arXiv: [astro-ph/0007354](https://arxiv.org/abs/astro-ph/0007354) [astro-ph] (July 2001).
84. Yahil, A. & Vidal, N. V. The Velocity Distribution of Galaxies in Clusters. **214**, 347–350 (June 1977).
85. Zwicky, F. On the Masses of Nebulae and of Clusters of Nebulae. **86**, 217 (Oct. 1937).